

Unraveling the Atmospheric Energy Input and Ionization due to EMIC-Driven Electron Precipitation from ELFIN Observations

L. Capannolo^{1*}, R. Marshall², W. Li¹, G. Berland², K. Duderstadt³, N. Sivadas^{4,5}, D. L. Turner⁶, and V. Angelopoulos⁷

¹ Center for Space Physics, Boston University, Boston, MA, USA

² Department of Aerospace Engineering Sciences, University of Colorado Boulder, Boulder, CO, USA

³ Earth Systems Research Center, The University of New Hampshire, Durham, NH, USA

⁴ Space Weather Laboratory, NASA Goddard Space Flight Center, Greenbelt, MD, USA

⁵ Department of Physics, The Catholic University of America, Washington DC, MD, USA

⁶ Space Exploration Sector, Johns Hopkins University Applied Physics Laboratory: Laurel, MD, USA

⁷ Department of Atmospheric and Oceanic Sciences, University of California, Los Angeles, CA.

Corresponding author: Luisa Capannolo (luisacap@bu.edu)

Key Points:

- ELFIN's pitch-angle resolved data provide an ideal input to the BERI model to estimate atmospheric ionization due to electron precipitation
- EMIC-driven precipitation occurs at all longitudes and 50°–70° latitudes; 74% of its input energy flux efficiently ionizes the atmosphere
- Ionization is enhanced in the mesosphere at altitudes ranging from 52 to 74 km, with ionization rates of ~100–200 pairs/cm³/s

Abstract

Energetic electron precipitation (EEP) from the radiation belts into Earth's atmosphere leads to several profound effects (e.g., enhancement of ionospheric conductivity, possible acceleration of ozone destruction processes). An accurate quantification of the energy input and ionization due to EEP is still lacking due to instrument limitations of low-Earth-orbit satellites capable of detecting EEP. The deployment of the ELFIN CubeSats marks a new era of observations of EEP with an improved pitch-angle (0° – 180°) and energy (50 keV–6 MeV) resolution. Here, we focus on the EEP recorded by ELFIN coincident with electromagnetic ion cyclotron (EMIC) waves, which play a major role in radiation belt electron losses. The EMIC-driven EEP (~ 200 keV– ~ 2 MeV) exhibits a pitch-angle distribution (PAD) that flattens with increasing energy, indicating a more efficient high-energy precipitation. Leveraging the combination of unique electron measurements from ELFIN and a comprehensive ionization model known as the Boulder Electron Radiation to Ionization (BERI), we quantify the energy input of EMIC-driven precipitation (on average, $\sim 3.3 \times 10^{-2}$ erg/cm²/s), identify its location (any longitude, 50° – 70° latitude), and provide the expected range of ion-electron production rate (on average, 100–200 pairs/cm³/s), peaking in the mesosphere – a region often overlooked. Our findings are crucial for improving our understanding of the magnetosphere-ionosphere-atmosphere system as they accurately specify the contribution of EMIC-driven EEP, which serves as crucial inputs to state-of-the-art atmospheric models (e.g., WACCM), to quantify the accurate impact of EMIC waves on both the atmospheric chemistry and dynamics.

Plain Language Summary

Energetic electron precipitation (EEP) from Earth's radiation belts is a source of energy input to the terrestrial atmospheric system and has the potential of impacting its chemistry and possibly dynamics. Available datasets of EEP are incomplete due to instrumental limitations, hindering the accurate quantification of EEP energy input, its properties, and the resulting ionization. Here, we leverage the observations of the ELFIN CubeSats which provide high-resolution data for the first time both in energy and look-direction (pitch-angle). We specifically focus on observations during electromagnetic ion cyclotron (EMIC) waves, known to precipitate the most energetic electrons, thus penetrating the atmosphere at low altitudes. We estimate the EMIC-driven EEP energy input and its resulting ion-electron production rate as a function of altitude using a sophisticated method that takes into account the EEP pitch-angle distribution. We find that 74% of the energy input ionizes the atmosphere, primarily in the mesosphere (peaking between 52–74 km), a region currently underestimated by recent ionization rate recommendations. We provide the region where EMIC-driven EEP is observed and the ionization rates at each location, which can be used as input to comprehensive atmospheric models to ultimately quantify the accurate impact of EMIC waves on Earth's atmosphere.

1 Introduction

Wave-particle interactions (e.g., Thorne, 2010; Li & Hudson, 2019) and field line scattering (e.g., Capannolo et al., 2022a; Sivasdas et al., 2019; Sergeev et al., 1983, 1983; Yahnin et al., 2016, 2017) often occur in Earth's magnetosphere and precipitate electrons and ions into the atmosphere. Here, particles interact with the ambient neutral molecules, depositing their energy into the system. The higher the particle energy, the deeper into the atmosphere the particle will deposit most of its energy, producing a variable number of ion-electron pairs (ionization rate or production rate) along its trajectory (i.e., altitude) (e.g., Roble & Ridley, 1987;

Fang et al., 2010; Lazarev, 1967). Figure 1A provides an illustration for this process. Recent studies have demonstrated that the ionization profile also depends on the pitch-angle distribution (PAD) of the impacting electrons (Marshall & Bortnik, 2018; Xu et al., 2018, 2020). At low altitudes (<50 km), secondary ionization effects induced by Bremsstrahlung photons are also important (Xu & Marshall, 2019; Xu et al., 2021).

Ionization due to energetic electron precipitation (EEP) has several effects on the atmospheric system. EEP can enhance the ionospheric density and conductivity (Robinson et al., 1987; Khazanov et al., 2018, 2021; Yu et al., 2018), which not only influences the reliability of communication systems (e.g., Booker & Wells, 1938; Cummer et al., 1998), but also affects the propagation of geomagnetic currents that link the magnetosphere to the atmosphere, critical to accurately model the entire geospace system (e.g., Peymirat & Fontaine, 1994; Korth et al., 2014; Xiong et al., 2020). On the other hand, ionization from EEP affects the atmospheric chemistry by increasing the concentration of nitrogen and hydrogen oxides (NO_x , HO_x), which act as catalysts of ozone (O_3) destruction (e.g., Sinnhuber et al., 2012; Meraner & Schmidt, 2018; Randall et al., 2005). This ozone depletion can occur either through local interaction (*direct effect*; Andersson et al., 2014; Zawedde et al., 2018) or via the subsequent transport of NO_x into the stratosphere during polar winters, with the potential for long-lasting effects (*indirect effect*; Hendry et al., 2021; Maliemi et al., 2020; Randall et al., 2006, 2007). In turn, ozone loss could accelerate the polar vortex, thus leading to changes in the radiative balance and possibly overall climate (Baumgaertner et al., 2011; Maliemi et al., 2019; Rozanov et al., 2012; Salminen et al., 2020). Finally, secondary ionization due to EEP reaches low altitudes, possibly even accounting for enhancements of radiation doses at airplane heights (Xu et al., 2021; Tobiska et al., 2016, 2018), together with showers induced by galactic cosmic rays (GCR). All these effects clearly highlight the importance of quantifying the energy input and impact of EEP.

Despite the extensive implications of EEP for the atmosphere, accurate quantification and inclusion of EEP in atmospheric models remain challenging, mainly due to the limitations imposed by instrument capabilities and their spatial coverage. While the input of solar energetic particles (SEP), GCR and auroral electrons has been recognized as important and quantified, electrons of radiation belt origin (>50 keV up to ~multi-MeV) have been almost entirely neglected. Studies show that NO_x and HO_x concentrations are underestimated if atmospheric models only include ionization due to SEP, GCR and auroral electrons (Andersson et al., 2018; Arsenovic et al., 2016; Duderstadt et al., 2021; Randall et al., 2015; Pettit et al., 2021). Only recently, the Coupled Model Intercomparison Project (CMIP6) included medium-energy electrons (MEE; Matthes et al., 2017) obtained from the POES/MetOp constellation of low-Earth-orbit (LEO) satellites orbiting at an altitude of 800–850 km (e.g., Evans & Greer, 2004; Sandanger et al., 2015; Rodger et al., 2010). EEP observations (zenith-oriented telescope, 0°) from three integral channels (E1: >30 keV, E2: >100 keV, E3: >300 keV) are parameterized with the Ap index (APEEP; van de Kamp et al., 2016) and used to calculate ionization rates through the methodology (valid until 1 MeV) based on Fang et al. (2010). Simulations show that such MEE contribution is crucial for improving the stratospheric response to ozone (Andersson et al., 2018).

Although POES provide extensive data (from 1998) and reasonable spatial coverage, the data suffer from several limitations (e.g., proton contamination, radiation damage, high noise levels, integral energy channels and very coarse energy steps). Different methods of data processing and calculations of ionization rates (Fang et al., 2010; Wissing & Kallenrode, 2009;

Rees, 1989) lead to variations of the production rates of at least one order of magnitude (Nesse Tyssoy et al., 2021), revealing that there is still a large uncertainty in the MEE ionization impact – an essential input to atmospheric models (Sinnhuber et al., 2021). Duderstadt et al. (2021) further investigated the EEP impact on ozone concentration by considering the full energy range of radiation belt electrons as input using data from the NASA Van Allen Probes (RBSP, Mauk et al., 2013; Spence et al., 2013), after scaling them to high-resolution observations from the FIREBIRD-II CubeSat (Johnson et al., 2020) during magnetic conjunctions. They focused on the 10-day-long electron loss occurring in March 2013 and showed that despite including MEE, the CMIP6 particle precipitation underestimated ozone loss in the mesosphere by 20%–40%, further motivating the community to account for the entire range of electron energy (>50 keV up to multi-MeV).

In this study, we quantify the energy input and ionization rates from EEP driven by EMIC (electromagnetic ion cyclotron) waves (0.1–5 Hz; Erlandson & Ukhorskiy, 2001; Fraser et al., 2010). EMIC waves are typically radially localized, but are more extended in magnetic local time (MLT) (e.g., Blum et al., 2017). In particular, EMIC-driven EEP is an important key loss process of radiation belt electrons (Drozdov et al., 2022; Shprits et al., 2017; Zhang et al. 2016). EMIC waves can indeed interact with electrons (e.g., Thorne, 2010) and precipitate them into the atmosphere, especially from post-noon to post-midnight (Carson et al., 2012; Gasque et al., 2021; Capannolo et al., 2022a). Precipitation has been observed by several LEO satellites or balloons (e.g., Blum et al., 2015; Hendry et al., 2016; Li et al., 2014; Woodger et al., 2018), and occurs frequently (on average, we calculated POES observes ~1–5 EEP events a day). EMIC waves scatter high-energy electrons more efficiently than low-energy ones, though the resulting EEP extends from ~100s keV up to ~MeV (e.g., Angelopoulos et al., 2023; Hendry et al., 2017; Capannolo et al., 2021, 2023). As a result, atmospheric ionization will be triggered over a broad range of altitudes, also extending at relatively low altitudes (due to the ~MeV electrons). Capannolo et al. (2023) analyzed 144 EMIC-driven EEP events observed by the Electron Losses and Fields Investigation (ELFIN) CubeSats (Angelopoulos et al., 2020). For the first time, ELFIN provided the electron PAD (0°–180°) at several differential energy channels, making these measurements the ideal input to the Boulder Electron Radiation to Ionization (BERI) model (Xu et al., 2020), which calculates the ionization profiles accounting for both electron energy and PAD. We evaluate how the production rates change as a function of altitude, energy, and pitch-angle and provide a map of the locations of precipitation events with associated ionization rates. Finally, we quantify the input energy flux resulting from the EMIC-driven precipitation events observed by ELFIN and the effective ionization production in the atmosphere as predicted by BERI.

2 Methodology

2.1 ELFIN CubeSats and the Dataset of EMIC-Driven Precipitation Events

The ELFIN CubeSat pair (3 sec spinning period, ~90 min orbital period at ~350–475 km of altitude) was launched in September 2019 and operated until its re-entry in mid-September 2022 (Angelopoulos et al., 2020). The CubeSats measured 50 keV–6 MeV electrons, from pitch-angles of 0° up to 180°. Compared to the commonly used POES/MetOp satellites, ELFIN offered significantly improved energy and pitch-angle resolution. ELFIN was able to observe electrons locally trapped (mirroring), precipitating (inside the bounce loss cone, LC; likely precipitated by some local mechanism like waves or field line scattering) and backscattered

(inside the anti-bounce-loss cone, ALC; likely due to atmospheric backscattering). Over the majority of its orbits (i.e., most latitudes and longitudes) at ~450 km altitude, ELFIN measures electrons that are entirely within the atmospheric loss cones (i.e., even electrons at 90° local pitch-angle are in the drift LC), thus they will be eventually lost to the atmosphere. We previously collected 144 EEP events driven by EMIC waves (details and analysis in Capannolo et al., 2023) using 10s–100s keV proton precipitation (observed by POES/MetOp nearby the ~MeV precipitation observed by ELFIN) as a proxy for EMIC waves (e.g., Capannolo et al., 2021; Carson et al., 2012; Miyoshi et al., 2008; Lyu et al., 2022). Capannolo et al. (2023) solely focused on the wave effects on electrons and the resulting local EEP, neglecting the consequent backscattered electrons. Backscattered electrons would either precipitate in the opposite hemisphere (i.e., ALC) or become quasi-trapped (i.e., drift LC) and eventually precipitate, albeit not local to the ELFIN location, but further eastward along the electron drift shells. On average, Capannolo et al. (2023) showed that EMIC-driven precipitation is observed on localized scales ($\Delta L \sim 0.3$) over 15–24 MLT and 5–8 L shells. The scattering efficiency rises with increasing energy, and PAD within the loss cone becomes flatter as energy increases, consistent with the understanding that EMIC waves primarily precipitate high-energy electrons (> 1 MeV). Low-energy electrons (down to ~200 keV) are precipitated as well, though less efficiently (e.g., Angelopoulos et al., 2023; Capannolo et al., 2021; Hendry et al., 2017). ELFIN’s energy and pitch-angle resolution provides an unprecedented opportunity to quantify the ionization effects resulting from the realistic PAD observed during EMIC wave activity. Here, we use the PAD as measured by ELFIN for each 144 EMIC-driven precipitation events and use it as input to the BERI model, which is described in Section 2.2. Given the field-of-view width of the pitch-angle sectors (22.5°), fluxes at pitch-angles close to the local LC angle measure mixed population (partly precipitating and partly trapped), making fluxes measured in this transition region not entirely reliable. To account for this, we exclude fluxes at pitch-angles within $\pm 22.5^\circ$ from the local LC angle and extrapolate their values using the flux at the nearest pitch-angle (outside the $\pm 22.5^\circ$ range from the LC angle).

2.2 BERI Model

The Boulder Electron Radiation to Ionization (BERI) model was developed by Xu et al. (2020) to simulate the electron precipitation effects. It builds on models previously developed and validated at CU Boulder (e.g., Marshall & Bortnik, 2018; Marshall et al., 2014, 2019; Xu et al., 2018; Xu & Marshall, 2019), based on the energetic precipitation Monte Carlo (EPMC) model described in Lehtinen et al. (1999). BERI considers as input an arbitrary background mass density profile and an electron PAD defined for each electron energy at an altitude of 500 km. In this study, we use the NRLMSIS2 (Naval Research Laboratory Mass Spectrometer and Incoherent Scatter; Emmert et al., 2020) model for the atmospheric density profile (Python package developed by Lucas, 2023) and the PAD observed by ELFIN for the 144 events associated with EMIC wave activity. As output, BERI provides the ion-electron pair production rate as a function of atmospheric altitude, which is calculated from the energy deposition, assuming that an energy of 35 eV is needed to produce an ion-electron pair on average (Rees, 1989, p. 40; Berland et al., 2023). The magnetic field is assumed along zenith with a magnitude of ~40,000 nT (as measured at Poker Flat in Alaska at 700 km at night). The LC angle is ~66° at 500 km (defined by a mirror altitude of 100 km). The key advantages of using BERI are: (1) inclusion of the pitch-angle dependence of the downward-going electrons and (2) increased computational efficiency of the ionization profiles through the use of a lookup table, which

provides the atmospheric ionization response to electrons at different pitch-angles (0° – 90° , 1° resolution) and energies (3 keV–3 MeV, uniformly spaced in a logarithmic scale). Extensive validation tests are described in Xu et al. (2020) which demonstrate that BERI reliably converts satellite observations to ionization production rates, needed as crucial inputs for atmospheric chemistry models.

3 Results

3.1 Quantification of the Atmospheric Ionization

In this section, we compare the ionization rates from ELFIN's high-resolution PAD and POES low-resolution PAD using the dataset analyzed in Capannolo et al. (2023). We illustrate the average ionization rates due to the realistic PAD observed by ELFIN during EMIC wave activity and put these in context with the current CMIP6 recommendations for atmospheric modeling.

3.1.1 Comparison During an ELFIN&MetOp Conjunction

On 2 February 2021, ELFIN-A observed EMIC-driven precipitation at $L \sim 4.8$ and $MLT \sim 19.4$ at $\sim 01:59:30$ UT, lasting ~ 30 s. Five minutes later, MetOp-02 observed both proton and electron precipitation (a tell-tale signature of EMIC wave activity; e.g., Capannolo et al., 2019a; Miyoshi et al., 2008) in a very similar L-MLT region ($\lesssim 0.3$ L and $\lesssim 2.3$ MLT). As the two satellites crossed a similar region within a few minutes of each other (i.e., magnetic conjunction; Figure 1B), it is likely that they observed the same or very similar patch of precipitation driven by EMIC waves since EMIC waves last much longer than a few minutes (e.g., Clausen et al., 2011; Blum et al., 2017). ELFIN PADs at three energy ranges are shown in Figure 1C–1E and POES proton and electron fluxes are illustrated in Figure 1F–1G, with a purple bar indicating the precipitation interval. Further details on this event are described in Capannolo et al. (2023). While ELFIN measured significant fluxes from 63 keV up to 2.9 MeV observing the full electron pitch-angle distribution (Figure 2A), MetOp only observed deep inside (pitch-angle of $\sim 27^\circ$, mapped to ELFIN's altitude using a dipole approximation) and outside ($\sim 90^\circ$) the local bounce LC in four integral energy channels (>30 keV, >100 keV, >300 keV, >700 keV). We examine the atmospheric ionization using BERI. To use BERI, MetOp data (integral electron flux) required a conversion to a PAD of differential number flux, calculated with the Peck et al. (2015) method, which considers both the 0° and 90° POES telescopes. Figures 2A–2B display the PADs for ELFIN and MetOp during the EMIC-driven precipitation event, respectively. The LC angle is indicated by a vertical dashed line. Figures 2C–2D show the PADs for ELFIN and MetOp (logarithmically) interpolated to the resolution of the BERI lookup table, respectively. Since proton precipitation in the >30 keV and >100 keV electron channels was strong during this event, the energy range analyzed is from ~ 300 keV to 1.4 MeV, based on the Peck et al. (2015) routine applied to MetOp observations. Note that while ELFIN's observations provide a high pitch-angle resolution, MetOp's PAD is interpolated from only 8 true measurements of integral electron fluxes, and is therefore likely to be less accurate than ELFIN's. Using the background atmospheric neutral density (Figure 2E) at the locations of ELFIN (black) and MetOp (blue), we provide the BERI ionization rates in Figure 2F. The profiles exhibit similar peaks (different by ~ 27 pairs/cm³/s) and altitudes of peak ionization (~ 4 km apart). These minor discrepancies are attributed to the different PADs used as inputs to BERI. Compared to ELFIN, MetOp observed a larger contribution of low-energy electrons, resulting in energy deposition at higher altitudes.

Additionally, the instrumental noise level of POES/MetOp is relatively high, thus high-energy precipitation might be underestimated (e.g., Nesse Tyssoy et al., 2016), possibly explaining why the high-energy flux observed by ELFIN is approximately twice that observed by MetOp. Consequently, electrons observed by ELFIN can deposit their energy at a lower altitude than those observed by MetOp. Although the shape and magnitude of the ion pair production profiles in Figure 2E are similar, ELFIN's resolution within the LC likely provides more accurate profiles.

3.1.2 Statistical Ionization Rates: Dependence on Altitude, Energy, Pitch-Angle, and Location

To calculate the expected atmospheric ionization rate due to EMIC-driven EEP, we binned the PAD into 10° pitch-angle bins for each event in the dataset and for each energy, from 63 keV up to 2.1 MeV, and calculated the average values (Figure 3A). Although ELFIN can observe electrons up to 6 MeV, the count rates in high energy channels are low, resulting in a limited statistical significance; therefore, we limit the PAD to 2.1 MeV. The average PAD in logarithmic scale was then interpolated to the pitch-angle and energy resolution in the lookup table (Figure 3B). Figure 3C further characterizes the precipitation input by displaying the PAD of differential energy flux. At low pitch-angles, the LC is more filled by high-energy electrons (≥ 300 keV) and the PAD flattens as energy increases. Both features are a consequence of more efficient scattering for high-energy electrons than low-energy electrons, consistent with EMIC waves as the driver of this precipitation. The atmospheric density profile is averaged from the atmospheric density of each event (Figure 3D).

Figure 4 highlights the energy and pitch-angle dependence of the ionization rates, given the average EMIC-driven PAD (Figure 3B). Figure 4A shows the ionization profile for monoenergetic electrons (color-coded in the legend) considering the contribution from all pitch-angles. Figure 4B illustrates the dependence on energy of the ionization peak (black) and its associated altitude (blue). As expected (e.g., Xu et al., 2020), high-energy electrons precipitate much deeper into the atmosphere, while low-energy electrons deposit their energy at higher altitudes. The altitude of the ionization peak decreases by ~ 22 km per decade in energy. Additionally, due to the characteristics of the PAD observed by ELFIN (flatter for high-energy electrons), the ionization rate peaks at higher values for high-energy electrons, since there is more contribution of precipitation at these energies. Figures 4C-4D show the variability of the ionization profiles given a specific pitch-angle (color-coded in the legend) considering the realistic PAD (Figure 3B) and the contribution from all energies. Electrons with lower pitch-angles tend to penetrate deeper into the atmosphere and ionize it at lower altitudes than electrons with higher pitch-angles, as the latter encounter a longer effective path through the atmosphere (Marshall & Bortnik, 2018). Electrons outside the loss cone ($\geq 66^\circ$) very rarely reach below 100 km altitude in the atmosphere, thus their ionization rates are negligible. The ionization peak reaches the maximum at the LC edge ($\sim 60^\circ$), given that the energy input is highest at this boundary (not shown). The ionization peak variability with pitch-angle in altitude (~ 7 km) and production rate (from ~ 2 to ~ 5 pairs/cm³/s) is less evident than the dependence on electron energy, suggesting that the ionization rates depend more on the electron energy and less on their pitch-angle. However, Figures 4C-4D highlight that different pitch-angles can affect different altitudes, thus an accurate input is preferred to provide the most realistic estimates.

Figure 5A illustrates the variability of the total ionization rates resulting from the 144 EMIC-driven EEP events observed by ELFEN. Different statistical calculations of the PAD are presented (mean, quartiles, min, max), with each line representing the associated ionization profile. The total ionization rate from the mean PAD is shown in black, with the dotted and dashed lines indicating its spread considering the standard error (σ/\sqrt{N} , where σ is the standard deviation in each pitch-angle bin and N is the number of data points in each pitch-angle bin, for a fixed energy). The quartiles of PAD are drawn in green: dashed line for the 25th, solid line for the 50th, and dotted line for the 75th. Additionally, we provide the possible range of ionization rates in blue: the minimum (solid) and maximum (dotted) ionization rates are calculated using the minimum and maximum PAD, respectively. The average atmospheric ionization peaks at 185 pairs/cm³/s (± 42 pairs/cm³/s) at 59 km, while the median ionization peaks at 70 pairs/cm³/s at the same altitude, suggesting that EMIC waves produce ionization of an order of 10^2 pairs/cm³/s. Furthermore, EMIC waves produce average ionization with rates ≥ 100 pairs/cm³/s over a broad altitude range (from ~ 52 km up to ~ 74 km), covering the entire extent of the mesosphere. Although the statistical significance of our dataset prevented the analysis to precipitation at energies below 2.1 MeV, EMIC waves also precipitate electrons at higher energies, potentially extending the altitude range even further, likely to $\lesssim 50$ km. We also provide an estimate of the energy deposition (energy flux per unit altitude), shown with the additional x-axes at the bottom of Figure 5A (maroon for eV/cm²/s/km and blue for erg/cm²/s/km). For this calculation, we assume that an energy of 35 eV is needed to produce an ion-electron pair on average (Rees, 1989, p. 40; Berland et al., 2023), and transform the pairs/cm³/s in energy flux per unit length, which is the ionization energy flux deposited at each km of altitude.

Supporting Figure S1 illustrates the distribution of the 144 EMIC-driven EEP events in geographic (A-B) and magnetic (C-D) coordinates, with their associated peak of ionization rate (Figure S1 A-C) and corresponding altitude (Figure S1 B-D). The event locations align with the extent of the outer radiation belt, as also shown in Capannolo et al. (2023), and demonstrate EMIC-driven precipitation occurs at any geographical longitude. Identifying the latitudinal and longitudinal location of EEP is valuable for specifying regional energy deposition and global extent in atmospheric models. It would be interesting to investigate whether the location of precipitation (both in latitude and longitude) impacts atmospheric model outputs (e.g., HO_x and NO_x production, O₃ reduction, neutral wind trends, etc.) and whether results are improved compared to models that rely on zonal (longitudinal) averages (Verronen et al., 2020).

3.1.3 Comparison with CMIP6 Recommendations

Here, we compare the ionization rates calculated with BERI due to EMIC-driven precipitation with those recommended by the CMIP6 (Matthes et al., 2017), which for the first time consider electron precipitation as an additional input of climate models. The solar forcing depends on solar variability and includes both radiative forcing (total solar and spectral solar irradiance and the F10.7 solar radio flux) and particle forcing from GCR, SEP, and MEE precipitation, parameterized with Ap and Kp indices (3-hour indices). This method also assumes that the electron energy is completely deposited into the atmosphere rather than being partly deposited and partly backscattered (as assumed in BERI). Note that the MEE input (van de Kamp et al., 2016) might underestimate the contribution of high-energy electrons, since the >700 keV POES electron channel is not directly included, and the Ap and Kp indices might not be a good proxy for MeV EEP (Hendry et al., 2021). Additionally, although measurements of high-energy EEP are frequent (on average, ~ 1 – 5 times a day for POES), they are impulsive in flux

and short-lived (~ 10 s seconds) due to the fast POES LEO orbit through the precipitation region. EEP generally lasts less than a day, probably several hours at most (the most prolonged recorded EMIC wave activity in situ lasted 8–10 hours; Blum et al., 2020; Engebretson et al., 2015). Moreover, EEP is detectable only if high-energy electrons are still populating the outer belt and have not been otherwise lost from the radiation belts, due to factors like magnetopause shadowing or persistent and strong EMIC wave scattering. As a result, the contribution of $\sim \text{MeV}$ EEP might be smoothed out in the daily averages of CMIP6. From the daily resolution of solar and particle forcing, we select the 144 days when EMIC-driven precipitation was observed by ELFIN and average the ionization rates at each altitude. We show these ionization rates in blue in Figure 5B, together with the rates calculated from BERI (in black and green for the average and median ELFIN PAD, respectively). At first glance, the ionization rates from BERI appear to be ~ 10 times higher than the MEE. However, BERI ionization rates are calculated specifically during the spatially localized and short-lived EMIC-driven precipitation when the precipitating fluxes are high. Since CMIP6 solar forcing is primarily intended for long-term studies, the MEE contribution is instead averaged on a daily basis, likely smoothing out short-lived precipitation. Consequently, caution should be exercised when making a one-to-one comparison of the ionization rates derived from BERI and MEE. The MEE contribution is substantial over 80–120 km, thus primarily impacts the D and E-regions of the ionosphere, but much reduced at lower altitudes. In contrast, BERI's estimates highlight that EMIC-driven precipitation primarily impacts the mesosphere, including the D-region ionosphere and possibly extending into the upper stratosphere, where the ozone concentration starts to rise. SEP also ionizes the mesosphere, but their impact becomes significant only during SEP events, which are less frequent compared to EMIC-driven EEP events.

This qualitative comparison demonstrates that accounting for accurate radiation belt precipitation is critical to obtain realistic ionization profiles at each atmospheric altitude, particularly in the mesosphere. Without BERI's estimates, CMIP6 recommendations would suggest that solar forcing is significant only above 80 km and below 30 km of altitude, overlooking the altitude range where high-energy electrons deposit the most energy. Note that the latitudes affected by these ionization rates are also different: MEE mostly precipitate in auroral latitudes, SEP are often observed at the poles and GCR are global. Therefore, direct comparisons of ionization rates should be made with caution, since each latitudinal region will be dominated by different energies of precipitation. Furthermore, EMIC-driven precipitation typically occurs on much shorter timescales than atmospheric circulation and climate, and it is still unclear if the cumulative effects of this short-lived precipitation could affect climate or only have localized and transitory effects during ongoing precipitation. In the future, we plan to explore if EMIC-driven ionization peaking in the mesosphere affects the atmospheric dynamics and chemistry on the short (\sim hours) or long (\sim days) timescales.

3.1.4 Comparing Ionization Rates based on a Realistic, Isotropic and Sinusoidal Energy-Pitch-Angle Distribution

Supporting Figures S2 and S3 compare the ionization rates assuming different PADs as input to the BERI model. The isotropic PAD assumption yields the highest ionization rate, as expected, since the LC is filled for all pitch-angles. The sinusoidal PAD provides an intermediate ionization rate, indicating that the realistic PAD falls off more rapidly than the sinusoidal PAD with decreasing pitch-angle within the loss cone. We find that, on average, the sinusoidal PAD produces ionization rates close to those from the more realistic PAD observed by ELFIN. For the

median, the isotropic PAD might be preferred in absence of high-resolution PAD from LEO satellite data, with the caveat that ionization rates might be slightly overestimated. Future work will assess whether these differences have a substantial effect on the outputs of atmospheric models, either on short or long timescales.

3.2 Estimate of the Energy Input during EMIC-Driven Precipitation and Corresponding Ionizing Energy Flux and Backscattered Energy Flux

Given the PAD of each of the 144 EMIC-driven events, we calculate the input energy flux ($\text{eV}/\text{cm}^2/\text{s}$) of downward-going electrons for each precipitation event by multiplying by the energy width of each ELFEN energy channel and integrating in pitch-angle and energy. We further calculate the energy flux responsible for ionizing the atmosphere by integrating the ionization profiles obtained with BERI across altitude, assuming that an energy of 35 eV is needed to produce an ion-electron pair on average (Rees, 1989, p. 40). The energy input for each event is shown on a latitude-longitude map in Figure 6 (A: from ELFEN's measurements; B: from BERI's ionization rates) in both $\text{eV}/\text{cm}^2/\text{s}$ (black) and $\text{erg}/\text{cm}^2/\text{s}$ (blue). Since part of the input energy flux measured by ELFEN is backscattered by the atmosphere, it is reasonable that the energy flux from BERI's estimates is lower. On average, EMIC-driven precipitation provides an input energy flux of $\sim 2.06 \times 10^{10} \text{ eV}/\text{cm}^2/\text{s}$ ($\sim 3.29 \times 10^{-2} \text{ erg}/\text{cm}^2/\text{s}$) in the LC (0° – 66°). The average ionization rates from BERI provide an energy flux of $\sim 1.53 \times 10^{10} \text{ eV}/\text{cm}^2/\text{s}$ ($\sim 2.45 \times 10^{-2} \text{ erg}/\text{cm}^2/\text{s}$), indicating that $\sim 74\%$ of the input energy flux is ionizing the atmosphere, while the rest is backscattered ($\sim 0.53 \times 10^{10} \text{ eV}/\text{cm}^2/\text{s}$, $\sim 0.84 \times 10^{-2} \text{ erg}/\text{cm}^2/\text{s}$). Figure 7 shows a cartoon of the energy budget due to local EMIC-driven precipitation: input and output energy fluxes are shown with the orange and pink arrows, respectively, and we show the effective atmospheric ionization due to such precipitation in white.

Furthermore, since ELFEN is also able to observe upward-going electrons, we can quantify the backscattered (anti-loss cone, ALC) energy flux during the EMIC-driven precipitation events and compare it with the values expected from BERI. On average, ELFEN observes an energy flux of $\sim 5.20 \times 10^{10} \text{ eV}/\text{cm}^2/\text{s}$ ($\sim 8.33 \times 10^{-2} \text{ erg}/\text{cm}^2/\text{s}$) for upward-going electrons (90° – 180°) and $\sim 0.74 \times 10^{10} \text{ eV}/\text{cm}^2/\text{s}$ ($\sim 1.18 \times 10^{-2} \text{ erg}/\text{cm}^2/\text{s}$) in the ALC (114° – 180°). The estimate of upward-going electrons from BERI's model is $\sim 5.18 \times 10^{10} \text{ eV}/\text{cm}^2/\text{s}$ ($\sim 8.29 \times 10^{-2} \text{ erg}/\text{cm}^2/\text{s}$), in agreement with ELFEN's observations, providing strong evidence that BERI accurately computes electron backscatter rates. We calculate BERI's backscattered energy flux either (1) by adding the energy flux that is not ionizing the atmosphere ($\sim 26\%$ of the LC energy flux from ELFEN) to the energy flux outside the LC (over 66° – 90°) measured by ELFEN or (2) by subtracting the energy flux ionizing the atmosphere estimated from BERI from the input energy flux from ELFEN. More in depth comparison with backscattering measurements is provided in Berland et al. (2023).

To compare the contribution from EMIC-driven precipitation with the contribution due to auroral precipitation estimated in Newell et al. (2009), we convert the observed input energy flux inside the LC to energy per unit time (power expressed in Watts). Considering a conservative extent of EMIC waves of $\sim 0.5 \text{ L}$ at $\sim 6.5 \text{ L}$ and $\sim 3 \text{ MLT}$ (corresponding to $\sim 1^\circ$ magnetic latitude and 45° magnetic longitude; Clausen et al., 2011; Blum et al., 2017; Hendry et al., 2020; Mann et al., 2014) and considering precipitation in both hemispheres, we estimate a total energy flux of $\sim 15 \text{ MW}$. Only $\sim 74\%$ of is expected to ionize the atmosphere ($\sim 11 \text{ MW}$). However, previous studies show that EMIC waves can persist for several hours and can extend over many MLT

sectors (e.g., Blum et al., 2020; Engebretson et al., 2015; Kim et al., 2016; Mann et al., 2014), though remain radially localized (Blum et al., 2017; Paulson et al., 2014; Mann et al., 2014), suggesting that EMIC-driven precipitation is indeed possible over wide longitudinal extents though narrower in latitudinal scales. This agrees with the spatial distribution of EMIC-driven precipitation events, as shown in Figure 6 and Figure S1. Thus, we can provide an upper limit of the EMIC-driven contribution of ~ 59 MW (with ionization estimated at ~ 44 MW). This calculation is derived under the assumption of the same latitudinal extent, but with a broader longitudinal range of $\sim 180^\circ$, corresponding to 12h in MLT – the upper MLT limit of EMIC waves observed by Engebretson et al. (2015). The actual EMIC-driven input power lies between these two bounds (15–59 MW), and it notably depends on the ongoing EMIC wave activity, including its intensity and spatial extent, as well as the resulting EEP occurring in specific geographical regions. Accurately quantifying the regional extent of EMIC waves and EMIC-driven precipitation poses a significant challenge, primarily due to limitations in equatorial and LEO satellite coverage. It requires a case-by-case analysis, relying on a combination of measurements from a constellation of spacecraft and ground-based networks (e.g., Hendry et al., 2020; Engebretson et al., 2015; Yahnin et al., 2021) and/or imaging of precipitation regions (e.g., Marshall et al., 2020). Furthermore, the specific input of EMIC-driven EEP can significantly vary over space and time and should be quantified case-by-case as it depends not only on the EMIC wave activity, but also on the radiation belt content (i.e., the outer radiation belt should be populated by enough electrons) and the resulting spatial extent of efficient EEP (i.e., where the resonance conditions are met). In summary, the estimated EMIC-driven power is lower than the auroral power estimated by Newell et al. (2009) (1–6 GW), as expected given the broader geographical extent of the aurora. However, while auroral precipitation mainly affects the E-region and partly the D-region of the ionosphere, EMIC waves are capable of scattering much more energetic electrons, which deposit their energy at lower altitudes. Additionally, auroral precipitation maps to much higher latitudes in comparison to EMIC-driven precipitation. Consequently, the atmospheric effects of these two phenomena may exhibit variations due to their distinct characteristics and geographical locations.

4 Discussion & Conclusions

In this study, we quantify the atmospheric ionization from EMIC wave-driven electron precipitation, utilizing the observations of 144 EMIC-driven EEP events from the ELFINS CubeSats from 2019 to 2022 (further described in Capannolo et al., 2023) as input to the BERI model (Xu et al., 2020). We provide the statistical PAD of EMIC-driven precipitation, its energy input, and its resulting ionization rates. EMIC-driven EEP exhibits a larger contribution of high-energy electrons compared to low-energy electrons because EMIC waves more efficiently scatter high-energy electrons. Due to the limited statistical significance at high energies, our results are valid for the energy range over 68 keV–1.932 MeV (or 63 keV–2.1 MeV from ELFINS's data). Our key findings are summarized and discussed below.

1. ELFINS data provides unprecedented measurements of precipitating electrons with high energy and pitch-angle resolution, which serve as ideal inputs to the BERI model, significantly enhancing the accuracy of ionization rate estimates.

We showed an example of the data quality comparison between POES and ELFINS (Section 3.1.1), highlighting that POES observations require multiple assumptions to remove proton contamination from low-energy electron measurements and to convert the measured

integral energy fluxes to the differential electron flux. The example also highlights the limitations of the POES detector in measuring low flux (Nesse Tyssoy et al., 2016), especially at high-energy, which in turns leads to a peak in ionization rates at a slightly higher altitude than what is estimated using the ELFIN data. Although the differences in ionization profiles are moderate, it remains unknown whether a small change in the altitude distribution of ionization substantially impacts the atmospheric chemistry and dynamics. Whenever available, we recommend using ELFIN data to estimate ionization rates since it offers improved resolution in energy and pitch-angle. However, ELFIN data has more constrained spatial and temporal coverage compared to the POES constellation. Therefore, we encourage the community to contemplate launching multiple ELFIN-like satellites into LEO, as single-point observations are insufficient to capture the spatiotemporal variability of EEP across the globe. In the meantime, careful comparison and cross-calibration between the ELFIN and POES spacecraft (e.g., during the numerous magnetic conjunctions) could allow us to potentially obtain a hybrid dataset that provides improved energy and pitch-angle resolution (from ELFIN's characteristics) and broad spatial and temporal coverage (from POES). Although this is a challenging task, it might provide a solution to accurately quantify atmospheric ionization over an extensive spatial coverage.

2. Electrons scattered by EMIC waves primarily deposit their energy in the mesosphere, with average values of $\sim 100\text{--}200$ pairs/cm³/s (over a broad altitude range of $\sim 52\text{--}74$ km) and energy deposition of $\sim 10^{-3}$ erg/cm²/s/km.

EMIC waves primarily scatter high-energy electrons, thus affect the D-region and altitudes below, potentially extending even into the stratosphere through Bremsstrahlung-induced secondary ionization (Xu et al., 2021; Berland et al., 2023). Our analysis provides an estimate of the average ionization profile and the possible range of ionization due to EMIC waves, which could serve as an input to atmospheric models to quantify the effect of EMIC-driven precipitation in the production of HO_x and NO_x and possible subsequent ozone depletion. Previous studies have shown that radiation belt electrons could have a substantial impact on the atmosphere's chemistry; thus, the contribution from EMIC-driven precipitation (i.e., the most energetic population) should not be excluded from consideration in atmospheric models. We have shown that the current CMIP6 recommendations are underestimating the contribution of high-energy EEP in the mesosphere.

3. For the events studied here, EMIC-driven precipitation averages: ~ 0.033 erg/cm²/s of input energy flux, ~ 0.025 erg/cm²/s of energy flux that ionizes the mesosphere, and ~ 0.008 erg/cm²/s energy flux of backscattered electrons. The input power of EMIC-driven precipitation is in the range of $\sim 15\text{--}59$ MW, depending on the area of precipitation (1° magnetic latitude extent and ranging from 45° to 180° magnetic longitude).

The energy input and the input power due to EMIC-driven precipitation are lower than those estimated for auroral precipitation (Newell et al., 2009). This is reasonable because aurora covers a much broader area than EMIC-driven precipitation and the low-energy electrons producing aurora are more abundant than those scattered by EMIC waves. However, it is important to emphasize that EMIC-driven precipitation affects both lower altitudes and lower magnetic latitudes ($\sim 56^\circ\text{--}68^\circ$) than the auroral precipitation ($>70^\circ$). Therefore, its effect on the atmospheric chemistry and dynamics is distinct from that of auroral precipitation. Our relatively limited dataset of EMIC-driven precipitation events demarcates a region where EMIC-driven precipitation is possible, however, does not allow us to infer the exact spatial or temporal extent

of the precipitation region. A combination of satellite and possibly ground-based measurements (e.g., Hendry et al., 2020; Engebretson et al., 2015; Yahnin et al., 2021) or imaging of precipitation (Marshall et al., 2020) would overcome this limitation and improve the estimate on the evolution in time and space of the precipitation region.

Furthermore, our analysis reveals that, in the absence of a realistic PAD (as provided by ELFIN), a sinusoidal PAD for EMIC-driven precipitation provides a reasonable assumption for average ionization rates. We also showed that, as expected, higher energy electrons and field-aligned electrons deposit their energy at 50–60 km, while electrons with lower energy and with pitch-angles closer to the loss cone impact higher altitudes. Moreover, while EMIC-driven precipitation is spatially localized in latitude and typically occurs over 50°–70° in latitude, it is observed over a much broader geographical longitude, due to EMIC waves being more extended in local time than radially. As an additional comparison, we demonstrated that BERI estimates an energy flux of backscattered electrons comparable to ELFIN's observations, opening a new line of research in accurate modeling and comparison of the PAD of backscattered electrons. Some progress has been made recently by Berland et al. (2023).

It is noteworthy that our estimates of energy flux and ionization can only account for the local precipitation driven by EMIC waves and disregard any other contributions due to drifting and backscattered electrons. In fact, electrons backscattered by the atmosphere, as predicted by BERI and previous models (e.g., Cotts et al., 2011; Marshall & Bortnik, 2018), with pitch-angles inside the ALC (symmetric to the LC) are expected to precipitate in the opposite hemisphere, thus providing some energy input there as well. From ELFIN's observations, the ALC (114°–180°) energy flux during EMIC-driven precipitation is ~36% of that in the LC, providing a total energy flux of $\sim 0.74 \times 10^{10}$ eV/cm²/s ($\sim 1.18 \times 10^{-2}$ erg/cm²/s). Additionally, at ELFIN's altitude, the electrons outside the LC and the ALC are likely only locally trapped or quasi-trapped in the drift LC (Tu et al., 2009), indicating that they will also eventually deposit energy into the atmosphere over an electron drift period. These estimates require further modeling and understanding that we leave as future work.

Pilot studies by Hendry et al. (2021) and Ozaki et al. (2022) evaluated the ozone depletion specifically due to EMIC-driven precipitation using modeling, such as 1D Sodankyla Ion and neutral Chemistry model (Verronen et al., 2005, 2016; Turunen et al., 2009) and a combination of observations, such as the SABER experiment board the TIMED satellite (Russel et al., 1999; Rong et al., 2009). While Hendry et al. (2021) estimated ozone depletions of up to ~10% (short-lived during Summer EEP and longer-lived during Winter), Ozaki et al. (2022) observed changes up to 60%, indicating that the effect of EMIC-driven precipitation on ozone depletion can be quite significant. Although these results are based on case studies, and a comprehensive analysis of the overall effects of EEP on the atmosphere as a whole, especially over long timescales, is still unavailable, they provide further evidence of the critical importance of incorporating and exploring the impact of EMIC-driven precipitation into the atmospheric system.

In summary, the analysis we presented in this paper provides a database of accurate ionization rates associated with each EEP, together with an average ion-electron pair production due to EMIC waves. These outcomes can serve as inputs to advanced models, such as WACCM, to assess the impact of EMIC-driven precipitation on the entire atmosphere. This assessment can encompass various aspects, including the concentration of HO_x, NO_x and ozone, as well as the resulting effects on its dynamics, both on short and long timescales. Efforts to extend our limited

knowledge on the temporal and spatial variation of the precipitation region are also worth pursuing to improve estimates on the EEP extent in latitude, longitude and duration. Through these efforts, we can strive towards a more precise and complete representation of the magnetosphere-ionosphere-atmosphere coupling and the Earth's atmospheric system itself, advancing our understanding of its underlying physical processes and ultimately enhancing the accuracy of atmospheric models.

Acknowledgments

Efforts at Boston University are supported by NSF grants AGS-2247265 and AGS-2019950 and NASA grants 80NSSC20K1270, 80NSSC20K0698, 80NSSC21K1312. RM and GB are supported by NASA grants 80NSSC19K0648 and 80NSSC20K1401. KD contributions are associated with NSF grant 1650738 and NASA NNX15AF66G. VA acknowledged NASA award NNX14AN68G, and NSF grants AGS-1242918 and AGS-2019914. The authors acknowledge all members of the ELFIN and POES/MetOp teams for providing data. The authors also acknowledge the project SOLIC (funded by the Federal Ministry of Education and Research in Germany), the team on "Scenarios of Future Solar Activity for Climate Modelling" at the International Space Science Institute (ISSI, Bern), the Project SOLID of the European Community's Seventh Framework Programme (FP7 2012), and the EU COST Action ES1005 (TOSCA) for providing CMIP6 recommendations. The authors also acknowledge the University of Colorado Space Weather Technology, Research and Education Center (SWx TREC) for providing the API to download MSIS atmospheric density. The authors declare no conflict of interest.

Open Research

ELFIN data are available at <https://data.elfin.ucla.edu/> and processed using SPEDAS routines specifically written for processing ELFIN data by the ELFIN UCLA team (Angelopoulos et al., 2019). POES/MetOp data are available at: <https://www.ncei.noaa.gov/data/poes-metop-space-environment-monitor/access/11b/v01r00/>. The dataset of the 144 EMIC-driven events is available at <https://doi.org/10.5281/zenodo.7697272>. The BERI code used to perform the calculations is at <https://doi.org/10.5281/zenodo.3945306>. We used the Python package at <https://github.com/SWxTREC/pymysis> to obtain the MSIS background atmosphere. CMIP6 recommendations are available at <https://solarisheppa.geomar.de/cmip6>. Data used to produce the figures is at <https://doi.org/10.5281/zenodo.8222649>. Data analysis was conducted using MATLAB. Figures 1A-1B and Figure 7 are created with Keynote for Mac OC.

References

- Andersson, M. E., Verronen, P. T., Marsh, D. R., Seppälä, A., Päivärinta, S.-M., Rodger, C. J., et al. (2018). Polar ozone response to energetic particle precipitation over decadal time scales: The role of medium-energy electrons. *Journal of Geophysical Research - D: Atmospheres*, 123, 607–622. <https://doi.org/10.1002/2017jd027605>
- Andersson, M. E., Verronen, P. T., Rodger, C. J., Clilverd, M. A., & Seppälä, A. (2014). Missing driver in the sun-Earth connection from energetic electron precipitation impacts mesospheric ozone. *Nature Communications*, 5(1), 5197. <https://doi.org/10.1038/ncomms6197>
- Angelopoulos, V., Cruce, P., Drozdov, A. et al. The Space Physics Environment Data Analysis System (SPEDAS). *Space Sci Rev* 215, 9 (2019). <https://doi.org/10.1007/s11214-018-0576-4>
- Angelopoulos, V., Tsai, E., Bingley, L. et al. The ELFING Mission. *Space Sci Rev* 216, 103 (2020). <https://doi.org/10.1007/s11214-020-00721-7>
- Angelopoulos, V., Zhang, XJ., Artemyev, A.V. et al. Energetic Electron Precipitation Driven by Electromagnetic Ion Cyclotron Waves from ELFING's Low Altitude Perspective. *Space Sci Rev* 219, 37 (2023). <https://doi.org/10.1007/s11214-023-00984-w>
- Arsenovic, P., Rozanov, E., Stenke, A., Funke, B., Wissing, J., Mursula, K., et al. (2016). The influence of middle range energy electrons on atmospheric chemistry and regional climate. *Journal of Atmospheric and Solar-Terrestrial Physics*, 149, 180–190. <https://doi.org/10.1016/j.jastp.2016.04.008>
- Baumgaertner, A. J. G., Seppälä, A., Jöckel, P., & Clilverd, M. A. (2011). Geomagnetic activity related NO_x enhancements and polar surface air temperature variability in a chemistry climate model: modulation of the NAM index. *Atmospheric Chemistry and Physics*, 11, 4521–4531. <https://doi.org/10.5194/acp-11-4521-2011>
- Berland, G., Marshall R. A., Capannolo L., McCarthy M., Zheng L. (2023), Kinetic Modeling of Radiation Belt Electrons with GEANT4 to Study Energetic Particle Precipitation in Earth's Atmosphere, *Earth and Space Science*, doi: 10.1029/2023EA002987.
- Blum, L. W., Bonnell, J. W., Agapitov, O., Paulson, K., and Kletzing, C. (2017), EMIC wave scale size in the inner magnetosphere: Observations from the dual Van Allen Probes, *Geophys. Res. Lett.*, 44, 1227– 1233, doi:10.1002/2016GL072316.
- Blum, L. W., Bonnell, J. W., Agapitov, O., Paulson, K., and Kletzing, C. (2017), EMIC wave scale size in the inner magnetosphere: Observations from the dual Van Allen Probes, *Geophys. Res. Lett.*, 44, 1227–1233, doi:10.1002/2016GL072316.
- Blum, L. W., Halford, A., Millan, R., Bonnell, J. W., Goldstein, J., Usanova, M., et al. (2015). Observations of coincident EMIC wave activity and duskside energetic electron precipitation on 18–19 January 2013. *Geophysical Research Letters*, 42, 5727–5735. <https://doi.org/10.1002/2015GL065245>
- Blum, L. W., Remya, B., Denton, M. H., & Schiller, Q. (2020). Persistent EMIC wave activity across the nightside inner magnetosphere. *Geophysical Research Letters*, 47, e2020GL087009. <https://doi.org/10.1029/2020GL087009>

- Booker, H. G., and Wells, H. W. (1938), Scattering of radio waves by the F-region of the ionosphere, *Terr. Magn. Atmos. Electr.*, 43(3), 249– 256, doi:10.1029/TE043i003p00249.
- Capannolo, L., Li, W., Millan, R., Smith, D., Sivadas, N., Sample, J., et al. (2022a). Relativistic Electron Precipitation Near Midnight: Drivers, Distribution, and Properties. *J. Geophys. Res. Space Phys.* 127, e2021JA030111. doi:10.1029/2021ja030111
- Capannolo, L., Li, W., Spence, H., Johnson, A. T., Shumko, M., Sample, J., & Klumpar, D. (2021). Energetic electron precipitation observed by FIREBIRD-II potentially driven by EMIC waves: Location, extent, and energy range from a multievent analysis. *Geophysical Research Letters*, 48, e2020GL091564. <https://doi.org/10.1029/2020GL091564>
- Capannolo, L., Li, W., Spence, H., Johnson, A. T., Shumko, M., Sample, J., & Klumpar, D. (2021). Energetic electron precipitation observed by FIREBIRD-II potentially driven by EMIC waves: Location, extent, and energy range from a multievent analysis. *Geophysical Research Letters*, 48, e2020GL091564. <https://doi.org/10.1029/2020GL091564>
- Capannolo, L., Li, W., Ma, Q., Shen, X. C., Zhang, X. J., Redmon, R. J., et al. (2019a). Energetic Electron Precipitation: Multievent Analysis of its Spatial Extent during EMIC Wave Activity. *J. Geophys. Res. Space Phys.* 124, 2466–2483. doi:10.1029/2018ja026291
- Capannolo, L., W. Li, Q. Ma, M. Qin, X.-C. Shen, V. Angelopoulos, A. Artemyev, X.-J. Zhang, M. Hanzelka. Electron Precipitation Observed by ELFIN Using Proton Precipitation as a Proxy for Electromagnetic Ion Cyclotron (EMIC) Waves; 2023; *Geophysical Research Letters*) - <https://doi.org/10.1029/2023GL103519>
- Carson, B. R., Rodger, C. J., & Clilverd, M. A. (2012). POES satellite observations of EMIC-wave driven relativistic electron precipitation during 1998–2010. *Journal of Geophysical Research: Space Physics*, 118, 232–243. <https://doi.org/10.1029/2012JA017998>
- Clausen, L. B. N., Baker, J. B. H., Ruohoniemi, J. M., and Singer, H. J. (2011), EMIC waves observed at geosynchronous orbit during solar minimum: Statistics and excitation, *J. Geophys. Res.*, 116, A10205, doi:10.1029/2011JA016823.
- Clausen, L. B. N., Baker, J. B. H., Ruohoniemi, J. M., and Singer, H. J. (2011), EMIC waves observed at geosynchronous orbit during solar minimum: Statistics and excitation, *J. Geophys. Res.*, 116, A10205, doi:10.1029/2011JA016823.
- Cotts, B. R. T., Inan, U. S., and Lehtinen, N. G. (2011), Longitudinal dependence of lightning-induced electron precipitation, *J. Geophys. Res.*, 116, A10206, doi:10.1029/2011JA016581.
- Cummer, S. A., Inan, U. S., and Bell, T. F. (1998), Ionospheric D-region remote sensing using VLF radio atmospherics, *Radio Sci.*, 33(6), 1781– 1792, doi:10.1029/98RS02381.
- Drozдов, A. Y., Aseev, N., Effenberger, F., Turner, D. L., Saikin, A., & Shprits, Y. (2019). Storm time depletions of multi-MeV radiation belt electrons observed at different pitch angles. *Journal of Geophysical Research: Space Physics*, 124, 8943– 8953. <https://doi.org/10.1029/2019JA027332>

- Duderstadt, K. A., Huang, C.-L., Spence, H. E., Smith, S., Blake, J. B., Crew, A. B., et al. (2021). Estimating the impacts of radiation belt electrons on atmospheric chemistry using FIREBIRD II and Van Allen Probes observations. *Journal of Geophysical Research: Atmospheres*, 126, e2020JD033098. <https://doi.org/10.1029/2020JD033098>
- Emmert, J. T., Drob, D. P., Picone, J. M., Siskind, D. E., Jones, M., Mlynczak, M. G., et al. (2021). NRLMSIS 2.0: A whole-atmosphere empirical model of temperature and neutral species densities. *Earth and Space Science*, 8, e2020EA001321. <https://doi.org/10.1029/2020EA001321>
- Engebretson, M. J., et al. (2015), Van Allen probes, NOAA, GOES, and ground observations of an intense EMIC wave event extending over 12 h in magnetic local time, *J. Geophys. Res. Space Physics*, 120, 5465–5488, doi:10.1002/2015JA021227.
- Erlandson, R. E., and A. J. Ukhorskiy (2001), Observations of electromagnetic ion cyclotron waves during geomagnetic storms: Wave occurrence and pitch angle scattering, *J. Geophys. Res.*, 106(A3), 3883–3895, doi:10.1029/2000JA000083.
- Evans, D. S., & Greer, M. S. (2004). Polar Orbiting Environmental Satellite Space Environment Moni-tor-2: Instrument descriptions and archive data documentation archive data documentation, NO-AA Technical Memorandum 93, Version 1.4. Boulder, CO: Space Weather Predict. Cent.
- Fang, X., Randall, C. E., Lummerzheim, D., Wang, W., Lu, G., Solomon, S. C., and Frahm, R. A. (2010), Parameterization of monoenergetic electron impact ionization, *Geophys. Res. Lett.*, 37, L22106, doi:10.1029/2010GL045406.
- Fraser, B. J., R. S. Grew, S. K. Morley, J. C. Green, H. J. Singer, T. M. Loto'aniu, and M. F. Thomsen (2010), Storm time observations of electromagnetic ion cyclotron waves at geosynchronous orbit: GOES results, *Journal of Geophysics Research*, 115, A05208, doi:10.1029/2009JA014516.
- Hendry, A. T., C. J. Rodger, and M. A. Clilverd (2017), Evidence of sub-MeV EMIC-driven electron precipitation, *Geophysical Research Letters*, 44, 1210–1218, doi:10.1002/2016GL071807.
- Hendry, A. T., Rodger, C. J., Clilverd, M. A., Engebretson, M. J., Mann, I. R., Lessard, M. R., et al. (2016). Confirmation of EMIC wave-driven relativistic electron precipitation. *Journal of Geophysical Research: Space Physics*, 121, 5366–5383. <https://doi.org/10.1002/2015JA022224>
- Hendry, A. T., Santolik, O., Miyoshi, Y., Matsuoka, A., Rodger, C. J., Clilverd, M. A., et al. (2020). A multi-instrument approach to determining the source-region extent of EEP-driving EMIC waves. *Geophysical Research Letters*, 47, e2019GL086599. <https://doi.org/10.1029/2019GL086599>
- Hendry, A. T., Seppälä, A., Rodger, C. J., & Clilverd, M. A. (2021). Impact of EMIC-wave driven electron precipitation on the radiation belts and the atmosphere. *Journal of Geophysical Research: Space Physics*, 126, e2020JA028671. <https://doi.org/10.1029/2020JA028671>
- Johnson, A. T., Shumko, M., Griffith, B., Klumpar, D. M., Sample, J., Springer, L., et al. (2020). The FIREBIRD-II CubeSat mission: Focused investigations of relativistic electron burst

intensity, range, and dynamics. *Review of Scientific Instruments*, 91, 034503.
<https://doi.org/10.1063/1.5137905>

Khazanov, G. V., Robinson, R. M., Zesta, E., Sibeck, D. G., Chu, M., & Grubbs, G. A. (2018). Impact of precipitating electrons and magnetosphere-ionosphere coupling processes on ionospheric conductance. *Space Weather*, 16, 829–837.
<https://doi.org/10.1029/2018SW001837>

Khazanov, G.V., Sibeck, D.G. and Chu, M. (2021). Magnetosphere–Ionosphere Coupling of Precipitating Electrons and Ionospheric Conductance. In *Magnetospheres in the Solar System* (eds R. Maggiolo, N. André, H. Hasegawa, D.T. Welling, Y. Zhang and L.J. Paxton). <https://doi.org/10.1002/9781119815624.ch16>

Kim, K.-H., Shiokawa, K., Mann, I. R., Park, J.-S., Kwon, H.-J., Hyun, K., Jin, H., and Connors, M. (2016), Longitudinal frequency variation of long-lasting EMIC Pc1-Pc2 waves localized in the inner magnetosphere, *Geophys. Res. Lett.*, 43, 1039–1046, doi:10.1002/2015GL067536.

Korth, H., Zhang, Y., Anderson, B. J., Sotirelis, T., and Waters, C. L. (2014), Statistical relationship between large-scale upward field-aligned currents and electron precipitation, *J. Geophys. Res. Space Physics*, 119, 6715–6731, doi:10.1002/2014JA019961.

Lazarev, V. (1967). Absorption of the energy of an electron beam in the upper atmosphere. *Geomagnetism and Aeronomy*, 7, 219.

Lehtinen, N. G., Bell, T. F., & Inan, U. S. (1999). Monte Carlo simulation of runaway MeV electron breakdown with application to red sprites and terrestrial gamma ray flashes. *Journal of Geophysical Research*, 104(A11), 24,699–24,712.
<https://doi.org/10.1029/1999JA900335>

Li, W., & Hudson, M. K. (2019). Earth's van Allen radiation belts: From discovery to the van Allen Probes era. *Journal of Geophysical Research: Space Physics*, 124, 8319–8351.
<https://doi.org/10.1029/2018JA025940>

Li, Z., Millan, R. M., Hudson, M. K., Woodger, L. A., Smith, D. M., Chen, Y., et al. (2014). Investigation of EMIC wave scattering as the cause for the BARREL 17 January 2013 relativistic electron precipitation event: A quantitative comparison of simulation with observations. *Geophysical Research Letters*, 41, 8722–8729.
<https://doi.org/10.1002/2014GL062273>

Lucas, Greg. (2023). *pymysis (v0.7.0)*. Zenodo. <https://doi.org/10.5281/zenodo.7581692>

Lyu, X., Ma, Q., Tu, W., Li, W., & Capannolo, L. (2022). Modeling the simultaneous dropout of energetic electrons and protons by EMIC wave scattering. *Geophysical Research Letters*, 49, e2022GL101041. <https://doi-org.ezproxy.bu.edu/10.1029/2022GL101041>

Maliniemi, V., Asikainen, T., Salminen, A., & Mursula, K. (2019). Assessing north Atlantic winter climate response to geomagnetic activity and solar irradiance variability. *The Quarterly Journal of the Royal Meteorological Society*, 145(725), 3780–3789.
<https://doi.org/10.1002/qj.365>

- Maliniemi, V., Marsh, D. R., Nesse Tyssøy, H., & Smith-Johnsen, C. (2020). Will climate change impact polar NO_x produced by energetic particle precipitation? *Geophysical Research Letters*, 47(9), e2020GL087041. <https://doi.org/10.1029/2020GL087041>
- Mann, I. R., Usanova, M. E., Murphy, K., Robertson, M. T., Milling, D. K., Kale, A., Kletzing, C., Wygant, J., Thaller, S., and Raita, T. (2014), Spatial localization and ducting of EMIC waves: Van Allen Probes and ground-based observations, *Geophys. Res. Lett.*, 41, 785–792, doi:10.1002/2013GL058581.
- Mann, I. R., Usanova, M. E., Murphy, K., Robertson, M. T., Milling, D. K., Kale, A., et al. (2014). Spatial localization and ducting of EMIC waves: Van Allen Probes and ground-based observations. *Geophysical Research Letters*, 41, 785–792. <https://doi.org/10.1002/2013GL058581>
- Marshall, R. A., & Bortnik, J. (2018). Pitch angle dependence of energetic electron precipitation: Energy deposition, backscatter, and the bounce loss cone. *Journal of Geophysical Research: Space Physics*, 123, 2412–2423. <https://doi.org/10.1002/2017JA024873>
- Marshall, R. A., Nicolls, M., Sanchez, E., Lehtinen, N. G., & Neilson, J. (2014). Diagnostics of an artificial relativistic electron beam interacting with the atmosphere. *Journal of Geophysical Research: Space Physics*, 119, 8560–8577. <https://doi.org/10.1002/2014JA020427>
- Marshall, R., Wei Xu, Thomas Woods, Christopher Cully, Allison Jaynes, Cora Randall, Daniel Baker, Michael McCarthy, Harlan E. Spence, Grant Berland, Alexandra Wold, Elliott Davis, The AEPEX mission: Imaging energetic particle precipitation in the atmosphere through its bremsstrahlung X-ray signatures, *Advances in Space Research*, Volume 66, Issue 1, 2020, Pages 66-82, ISSN 0273-1177, <https://doi.org/10.1016/j.asr.2020.03.003>. (<https://www.sciencedirect.com/science/article/pii/S0273117720301423>)
- Matthes, K., Funke, B., Andersson, M. E., Barnard, L., Beer, J., Charbonneau, P., Clilverd, M. A., Dudok de Wit, T., Haberreiter, M., Hendry, A., Jackman, C. H., Kretzschmar, M., Kruschke, T., Kunze, M., Langematz, U., Marsh, D. R., Maycock, A. C., Misios, S., Rodger, C. J., Scaife, A. A., Seppälä, A., Shangguan, M., Sinnhuber, M., Tourpali, K., Usoskin, I., van de Kamp, M., Verronen, P. T., and Versick, S.: Solar forcing for CMIP6 (v3.2), *Geosci. Model Dev.*, 10, 2247–2302, <https://doi.org/10.5194/gmd-10-2247-2017>, 2017.
- Mauk, B.H., Fox, N.J., Kanekal, S.G. et al. (2013), Science Objectives and Rationale for the Radiation Belt Storm Probes Mission, *Space Science Reviews*, 179: 3. <https://doi.org/10.1007/s11214-012-9908-y>.
- Meraner, K., & Schmidt, H. (2018). Climate impact of idealized winter polar mesospheric and stratospheric ozone losses as caused by energetic particle precipitation. *Atmospheric Chemistry and Physics*, 18, 1079–1089. <https://doi.org/10.5194/acp-18-1079-2018>
- Miyoshi, Y., Sakaguchi, K., Shiokawa, K., Evans, D., Albert, J., Connors, M., & Jordanova, V. (2008). Precipitation of radiation belt electrons by EMIC waves, observed from ground and space. *Geo-physical Research Letters*, 35, L23101. <https://doi.org/10.1029/2008GL035727>

- Miyoshi, Y., Sakaguchi, K., Shiokawa, K., Evans, D., Albert, J., Connors, M., & Jordanova, V. (2008). Precipitation of radiation belt electrons by EMIC waves, observed from ground and space. *Geo-physical Research Letters*, 35, L23101. <https://doi.org/10.1029/2008GL035727>
- Nesse Tyssøy, H., Sandanger, M. I., Ødegaard, L.-K. G., Stadsnes, J., Aasnes, A., and Zawedde, A. E. (2016), Energetic electron precipitation into the middle atmosphere—Constructing the loss cone fluxes from MEPED POES, *J. Geophys. Res. Space Physics*, 121, 5693–5707, doi:10.1002/2016JA022752.
- Nesse Tyssøy, H., Sandanger, M. I., Ødegaard, L.-K. G., Stadsnes, J., Aasnes, A., and Zawedde, A. E. (2016), Energetic electron precipitation into the middle atmosphere—Constructing the loss cone fluxes from MEPED POES, *J. Geophys. Res. Space Physics*, 121, 5693–5707, doi:10.1002/2016JA022752.
- Nesse Tyssøy, H., Sinnhuber, M., Asikainen, T., Bender, S., Clilverd, M. A., Funke, B., et al. (2021). HEPPA III intercomparison experiment on electron precipitation impacts: 1. Estimated ionization rates during a geomagnetic active period in April 2010. *Journal of Geophysical Research: Space Physics*, 126, e2021JA029128. <https://doi.org/10.1029/2021JA029128>
- Newell, P. T., Sotirelis, T., and Wing, S. (2009), Diffuse, monoenergetic, and broadband aurora: The global precipitation budget, *J. Geophys. Res.*, 114, A09207, doi:10.1029/2009JA014326.
- Peck, E. D., Randall, C. E., Green, J. C., Rodriguez, J. V., & Rodger, C. J. (2015). POES MEPED differential flux retrievals and electron channel contamination correction. *Journal of Geophysical Research: Space Physics*, 120, 4596–4612. <https://doi.org/10.1002/2014JA020817>
- Pettit, J. M., Randall, C. E., Peck, E. D., & Harvey, V. L. (2021). A new MEPED-based precipitating electron data set. *Journal of Geophysical Research: Space Physics*, 126, e2021JA029667. <https://doi.org/10.1029/2021JA029667>
- Peymirat, C., and Fontaine, D. (1994), Numerical simulation of magnetospheric convection including the effect of field-aligned currents and electron precipitation, *J. Geophys. Res.*, 99(A6), 11155–11176, doi:10.1029/93JA02546.
- Randall, C. E., and et al. (2005), Stratospheric effects of energetic particle precipitation in 2003–2004, *Geophys. Res. Lett.*, 32, L05802, doi:10.1029/2004GL022003.
- Randall, C. E., Harvey, V. L., Singleton, C. S., Bailey, S. M., Bernath, P. F., Codrescu, M., et al. (2007). Energetic particle precipitation effects on the Southern Hemisphere stratosphere in 1992–2005. *Journal of Geophysical Research: Atmospheres*, 112, D08308. <https://doi.org/10.1029/2006jd007696>
- Randall, C. E., Harvey, V. L., Singleton, C. S., Bernath, P. F., Boone, C. D., & Kozyra, J. U. (2006). Enhanced NO_x in 2006 linked to strong upper stratospheric Arctic vortex. *Geophysical Research Letters*, 33, L18811. <https://doi.org/10.1029/2006GL027160>
- Rees, M. H. (1989). *Physics and chemistry of the upper atmosphere*. New York: Cambridge Univ. Press.

- Robinson, R. M., Vondrak, R. R., Miller, K., Dabbs, T., and Hardy, D. (1987), On calculating ionospheric conductances from the flux and energy of precipitating electrons, *J. Geophys. Res.*, 92(A3), 2565– 2569, doi:10.1029/JA092iA03p02565.
- Roble, R. G., and E. C. Ridley (1987), An auroral model for the NCAR thermospheric general circulation model (TGCM), *Ann. Geophys.*, 5A(6), 369.
- Rodger, C. J., Clilverd, M. A., Green, J. C., & Lam, M. M. (2010). Use of POES SEM-2 observations to examine radiation belt dynamics and energetic electron precipitation into the atmosphere. *Journal of Geophysical Research*, 115, A04202. <https://doi.org/10.1029/2008JA014023>
- Rong, P. P., Russell, J. M., Mlynczak, M. G., Remsberg, E. E., Marshall, B. T., Gordley, L. L., & López-Puertas, M. Validation of thermosphere ionosphere mesosphere energetics and dynamics/sounding of the atmosphere using broadband emission radiometry (TIMED/SABER) v1.07 ozone at 9.6 μm in altitude range 15–70 km. *J. Geophys. Res.* 114, D04306. <https://doi.org/10.1029/2008JD010073> (2009).
- Rozanov, E., Calisto, M., Egorova, T., Peter, T., & Schmutz, W. (2012). Influence of the precipitating energetic particles on atmospheric chemistry and climate. *Surveys in Geophysics*, 33, 483–501. <https://doi.org/10.1007/s10712-012-9192-0>
- Russell, J. M. III, M. G. Mlynczak, L. L. Gordley, J. Tansock, and R. Esplin. An overview of the SABER experiment and preliminary calibration results. *Proc. SPIE* 3756, 277–288. <https://doi.org/10.1117/12.366382> (1999).
- Salminen, A., Asikainen, T., Maliniemi, V., & Mursula, K. (2020). Dependence of sudden stratospheric warmings on internal and external drivers. *Geophysical Research Letters*, 47(5), e2019GL086444. <https://doi.org/10.1029/2019GL086444>
- Sandanger, M. I., Ødegaard, L.-K. G., Nesse Tyssøy, H., Stadsnes, J., Søråas, F., Oksavik, K., & Aarsnes, K. (2015). In-flight calibration of NOAA POES proton detectors-Derivation of the MEPED correction factors. *Journal of Geophysical Research: Space Physics*, 120, 9578–9593. <https://doi.org/10.1002/2015JA021388>
- Sergeev, V. A., Malkov, M., & Mursula, K. (1993). Testing the isotropic boundary algorithm method to evaluate the magnetic field configuration in the tail. *Journal of Geophysical Research*, 98(A5), 7609–7620. <https://doi.org/10.1029/92JA02587>
- Sergeev, V. A., Sazhina, E. M., Tsyganenko, N. A., Lundblad, J., & S. raas, F. (1983). Pitch-angle scattering of energetic protons in the magnetotail current sheet as the dominant source of their isotropic precipitation into the nightside ionosphere. *Planetary and Space Science*, 31, 1147–1155. [https://doi.org/10.1016/0032-0633\(83\)90103-4](https://doi.org/10.1016/0032-0633(83)90103-4)
- Shprits, Y. Y., Kellerman, A., Aseev, N., Drozdov, A. Y., & Michaelis, I. (2017). Multi-MeV electron loss in the heart of the radiation belts. *Geophysical Research Letters*, 44, 1204–1209. <https://doi.org/10.1002/2016GL072258>
- Sinnhuber, M., Nieder, H., & Wieters, N. (2012). Energetic particle precipitation and the chemistry of the mesosphere/lower thermosphere. *Surveys in Geophysics*, 33(6), 1281–1334. <https://doi.org/10.1007/s10712-012-9201-3>

- Sivadas, N., Semeter, J., Nishimura, Y. T., & Mrak, S. (2019). Optical signatures of the outer radiation belt boundary. *Geophysical Research Letters*, 46, 8588–8596. <https://doi.org/10.1029/2019GL083908>
- Spence, H. E., Reeves, G. D., Baker, D. N., Blake, J. B., Bolton, M., Bourdarie, S., et al. (2013). Science goals and overview of the radiation belt storm probes (RBSP) energetic particle, composition, and thermal plasma (ECT) suite on NASA's Van Allen Probes mission. *Space Science Reviews*, 179(1–4), 311–336. https://doi.org/10.1007/978-1-4899-7433-4_10
- Thorne, R. M. (2010). Radiation belt dynamics: The importance of wave-particle interactions. *Geo-physical Research Letters*, 37, L22107. <https://doi.org/10.1029/2010GL044990>
- Tobiska, W. K., Didkovsky, L., Judge, K., Weiman, S., Bouwer, D., Bailey, J., et al. (2018). Analytical representations for characterizing the global aviation radiation environment based on model and measurement databases. *Space Weather*, 16, 1523–1538. <https://doi.org/10.1029/2018SW001843>
- Tobiska, W. K., et al. (2016), Global real-time dose measurements using the Automated Radiation Measurements for Aerospace Safety (ARMAS) system, *Space Weather*, 14, 1053–1080, doi:10.1002/2016SW001419.
- Tu, W., R. Selesnick, X. Li, and M. Looper (2010), Quantification of the precipitation loss of radiation belt electrons observed by SAMPEX, *J. Geophys. Res.*, 115, A07210, doi:10.1029/2009JA014949.
- Turunen, E., Verronen, P. T., Seppälä, A., Rodger, C. J., Clilverd, M. A., Tamminen, J., et al. (2009). Impact of different energies of precipitating particles on NO_x generation in the middle and upper atmosphere during geomagnetic storms. *Journal of Atmospheric and Solar-Terrestrial Physics*, 71(10), 1176–1189. <https://doi.org/10.1016/j.jastp.2008.07.005>
- van de Kamp, M., Seppälä, A., Clilverd, M. A., Rodger, C. J., Verronen, P. T., and Whittaker, I. C.: A model providing long- term datasets of energetic electron precipitation during geomagnetic storms, *J. Geophys. Res.-Atmos.*, 121, 12520–12540, <https://doi.org/10.1002/2015JD024212>, 2016.
- Verronen, P. T., Andersson, M. E., Marsh, D. R., Kovacs, T., & Plane, J. M. C. (2016). WACCM-D whole atmosphere community climate model with D-region ion chemistry. *Journal of Advances in Modeling Earth Systems*, 8, 954–975. <https://doi.org/10.1002/2015MS000592>
- Verronen, P. T., Marsh, D. R., Szélag, M. E., and Kalakoski, N.: Magnetic-local-time dependency of radiation belt electron precipitation: impact on ozone in the polar middle atmosphere, *Ann. Geophys.*, 38, 833–844, <https://doi.org/10.5194/angeo-38-833-2020>, 2020.
- Verronen, P. T., Seppälä, A., Clilverd, M. A., Rodger, C. J., Kyrölä, E., Enell, C.-F., et al. (2005). Diurnal variation of ozone depletion during the October-November 2003 solar proton events. *Journal of Geophysical Research*, 110, A09S32. <https://doi.org/10.1029/2004JA010932>
- Wissing, J. M., & Kallenrode, M.-B. (2009). Atmospheric ionization module osnabrück (aimos): A 3-d model to determine atmospheric ionization by energetic charged particles from

- different populations. *Journal of Geophysical Research: Space Physics*, 114(A6).
<https://doi.org/10.1029/2008ja013884>
- Woodger, L. A., Millan, R. M., Li, Z., & Sample, J. G. (2018). Impact of background magnetic field for EMIC wave-driven electron precipitation. *Journal of Geophysical Research: Space Physics*, 123, 8518–8532. <https://doi.org/10.1029/2018JA025315>
- Xiong, C., Stolle, C., Alken, P. et al. Relationship between large-scale ionospheric field-aligned currents and electron/ion precipitations: DMSP observations. *Earth Planets Space* 72, 147 (2020). <https://doi.org/10.1186/s40623-020-01286-z>
- Xu, W., & Marshall, R. A. (2019). Characteristics of energetic electron precipitation estimated from simulated bremsstrahlung X-ray distributions. *Journal of Geophysical Research: Space Physics*, 124, 2831–2843. <https://doi.org/10.1029/2018JA026273>
- Marshall, R. A., Xu, W., Sousa, A., McCarthy, M., & Millan, R. (2019). X-ray signatures of lightning-induced electron precipitation. *Journal of Geophysical Research: Space Physics*, 124, 10,230–10,245. <https://doi.org/10.1029/2019JA027044>
- Xu, W., & Marshall, R. A. (2019). Characteristics of energetic electron precipitation estimated from simulated bremsstrahlung X-ray distributions. *Journal of Geophysical Research: Space Physics*, 124, 2831– 2843. <https://doi.org/10.1029/2018JA026273>
- Xu, W., Marshall, R. A., & Tobiska, W. K. (2021). A method for calculating atmospheric radiation produced by relativistic electron precipitation. *Space Weather*, 19, e2021SW002735. <https://doi.org/10.1029/2021SW002735>
- Xu, W., Marshall, R. A., Fang, X., Turunen, E., & Kero, A. (2018). On the effects of bremsstrahlung radiation during energetic electron precipitation. *Geophysical Research Letters*, 45, 1167–1176. <https://doi.org/10.1002/2017GL076510>
- Xu, W., Marshall, R. A., Tyssøy, H. N., & Fang, X. (2020). A generalized method for calculating atmospheric ionization by energetic electron precipitation. *Journal of Geophysical Research: Space Physics*, 125, e2020JA028482. <https://doi.org/10.1029/2020JA028482>
- Yahnin A. G., T. A. Popova, A. G. Demekhov, A. A. Lubchich, A. Matsuoka, K. Asamura, Y. Miyoshi, S. Yokota, S. Kasahara, K. Keika, T. Hori, F. Tsuchiya, A. Kumamoto, Y. Kasahara, M. Shoji, Y. Kasaba, S. Nakamura, I. Shinohara, H. Kim, S. Noh, T. Raita, Evening Side EMIC Waves and Related Proton Precipitation Induced by a Substorm, *Journal of Geophysical Research: Space Physics*, 10.1029/2020JA029091, 126, 7, (2021).
- Yahnin, A. G., Yahnina, T. A., Raita, T., & Manninen, J. (2017). Ground pulsation magnetometer observations conjugated with relativistic electron precipitation. *Journal of Geophysics Research: Space Physics*, 122, 9169–9182.
<https://doi.org/10.1002/2017JA024249>
- Yahnin, A. G., Yahnina, T. A., Semenova, N. V., Gvozdevsky, B. B., & Pashin, A. B. (2016). Relativistic electron precipitation as seen by NOAA POES. *Journal of Geophysics Research: Space Physics*, 121, 8286–8299. <https://doi.org/10.1002/2016JA022765>
- Yu, Y., Jordanova, V. K., McGranaghan, R. M., & Solomon, S. C. (2018). Self-consistent modeling of electron precipitation and responses in the ionosphere: Application to low-altitude energization during substorms. *Geophysical Research Letters*, 45, 6371– 6381.
<https://doi.org/10.1029/2018GL078828>

- 958 Zawedde, A. E., Nesse Tyssøy, H., Stadsnes, J., & Sandanger, M. I. (2018). The impact of
959 energetic particle precipitation on mesospheric oh – Variability of the sources and the
960 background atmosphere. *Journal of Geophysical Research: Space*, 123(7), 5764–5789.
961 <https://doi.org/10.1029/2017JA025038>
- 962 Zhang, X.-J., Li, W., Ma, Q., Thorne, R. M., Angelopoulos, V., Bortnik, J., et al. (2016a). Direct
963 evidence for EMIC wave scattering of relativistic electrons in space. *Journal of*
964 *Geophysics Research: Space Physics*, 121, 6620–6631.
965 <https://doi.org/10.1002/2016JA022521>
966

Figure 1: A: Illustration of the different altitudes where energetic particles ionize the atmosphere; the radiation belt precipitation is marked in purple. B: overview of the geometry of the ELFIN&MetOp magnetic conjunction and diagram of electron precipitation (purple arrow) resulting from wave-particle interactions in the outer radiation belt; LEO satellite orbits are shown in blue (ELFIN) and green (MetOp); their intersection determines the magnetic conjunction, which occurs nearby the electron precipitation. C–G: figure adapted from Capannolo et al. (2023), which depicts the observations during the ELFIN&MetOp conjunction. C–E: PAD observed by ELFIN at 3 different energy intervals; solid (dashed) horizontal lines indicate the local loss (anti-loss) cone; the precipitation is highlighted with a purple bar. F–G: proton and electron flux observed by MetOp in conjunction with ELFIN; solid (dotted) lines indicate the precipitating (trapped) particles; the precipitation of both protons and electrons is highlighted with a purple bar.

Figure 2: Ionization rates during the EMIC-driven EEP event observed during the ELFIN&MetOp conjunction (Figure 1C–G). A–B: PADs from (A) ELFIN-A data and (B) MetOp-02 data processed with the Peck et al. (2015) routine, color-coded by energy; C–D: PADs interpolated to the BERI lookup table resolution; E: background atmospheric density at the satellite locations (ELFIN: black, MetOp: blue); F: ionization rates from BERI for each satellite (ELFIN: black, MetOp: blue). The loss cone at 500 km is indicated by the vertical dashed line in A, B, C, D.

Figure 3: Inputs to BERI model. A: PAD from statistical EMIC-driven EEP data (from ELFIN), color-coded by the center energies in each energy channel; B: PAD interpolated to the lookup table resolution, color-coded by energy; C: PAD for the energy flux from the PAD in B; D: background density for each event (black) and averaged at each altitude (red).

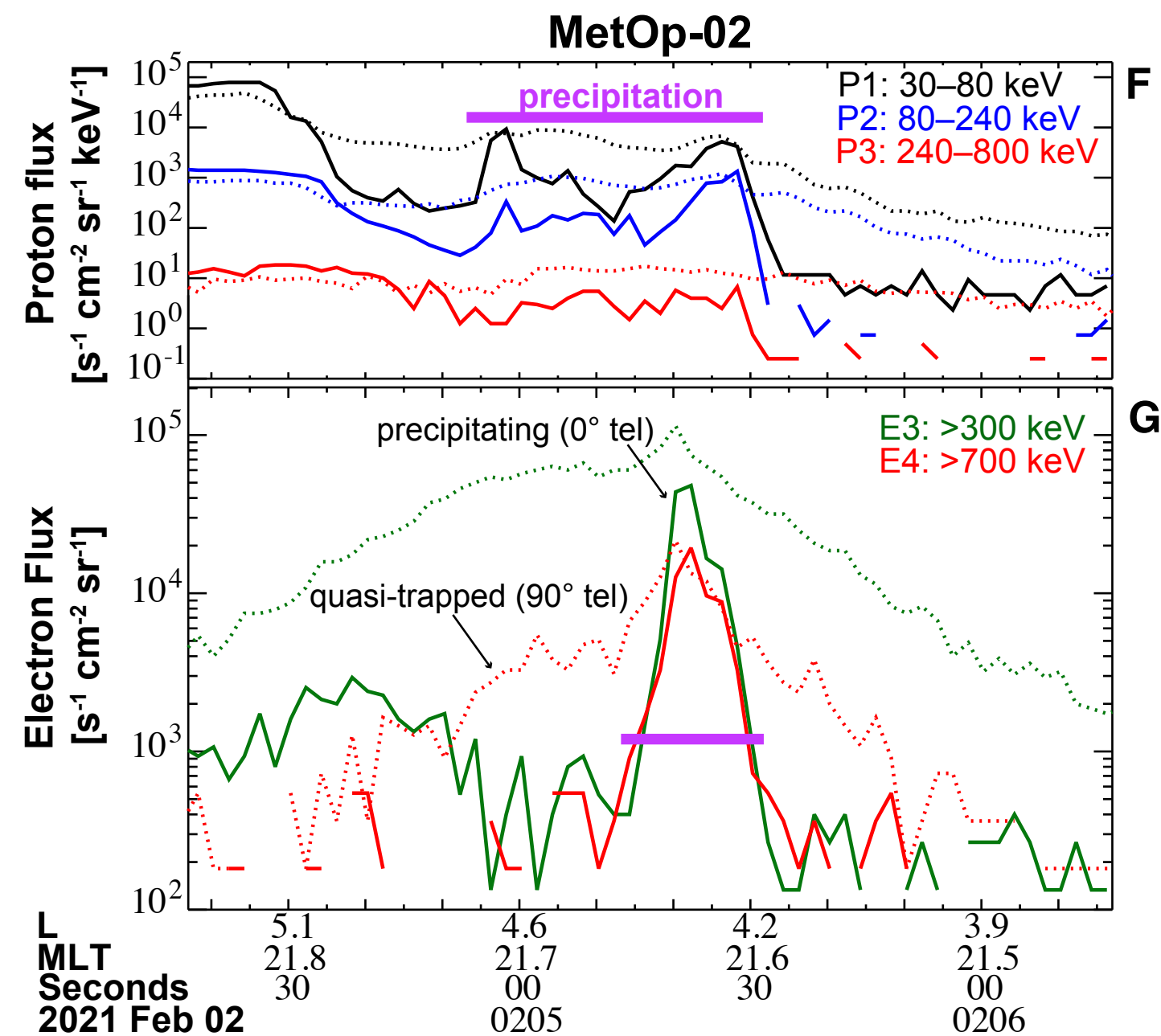
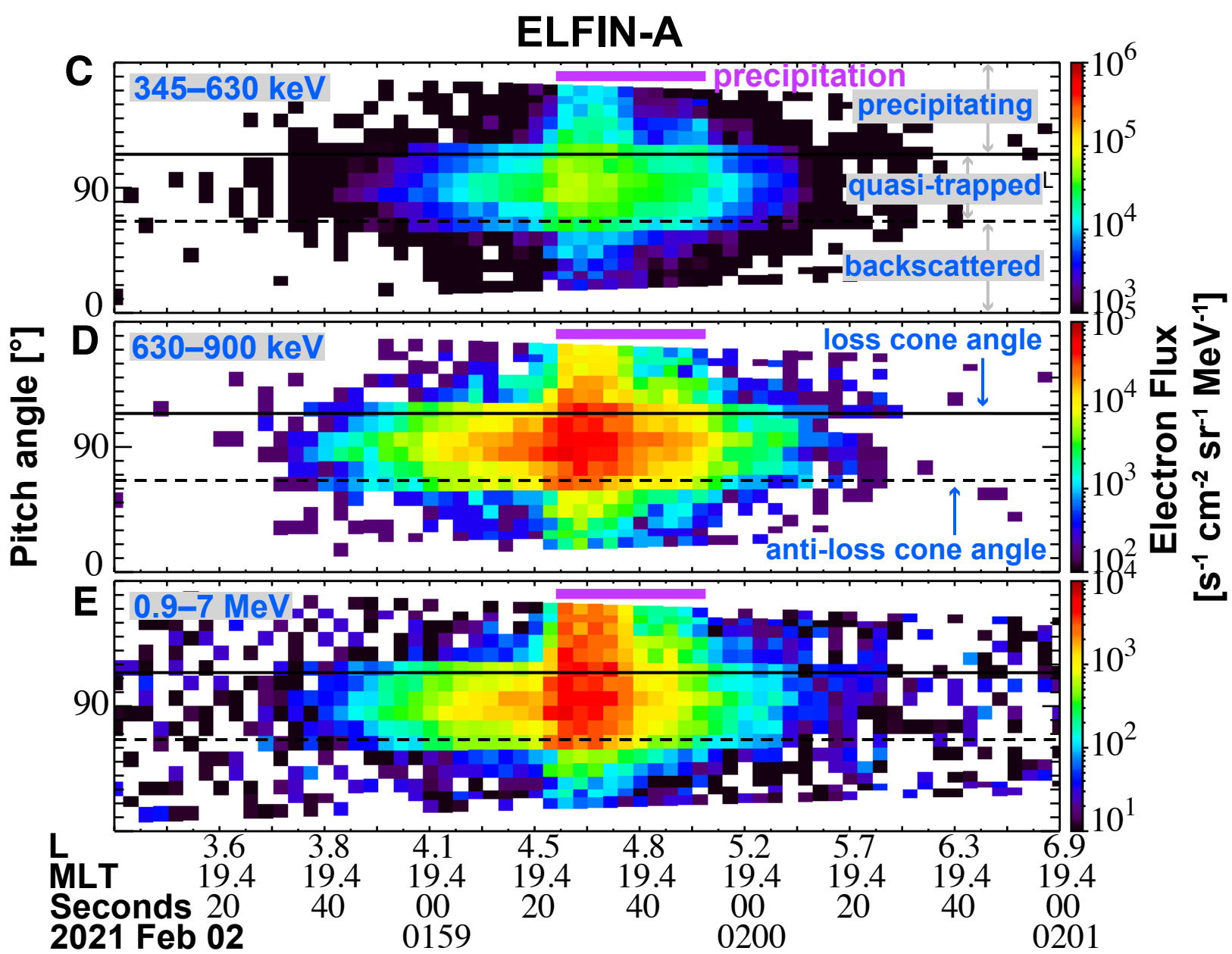
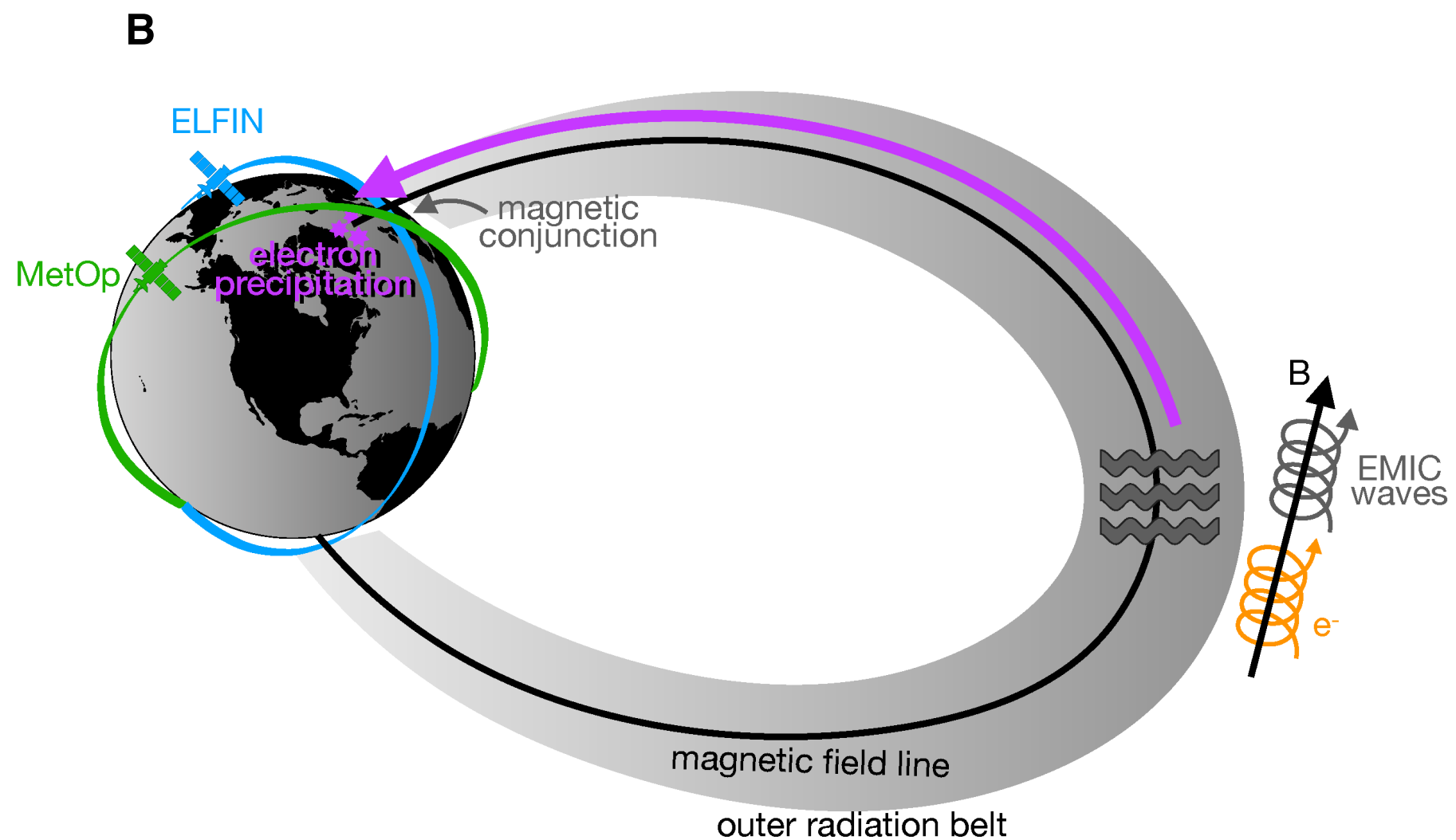
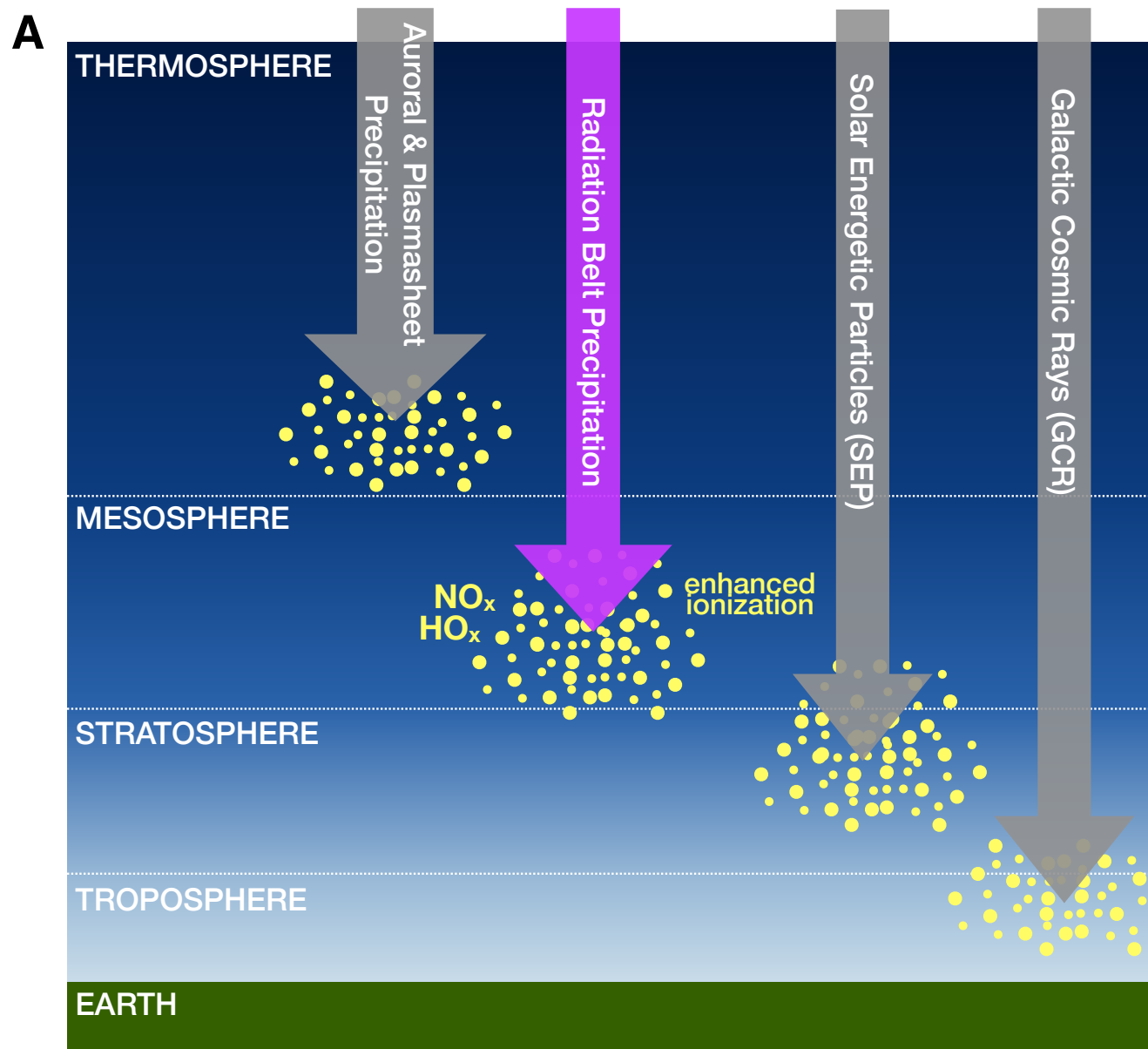
Figure 4: Dependence of the BERI ionization rates in energy (A–B) and pitch-angle (C–D). Ionization rates for a fixed electron energy (A) and pitch-angle (C). Peak of ionization rate (black) and corresponding altitude (blue) as a function of energy (B) and pitch-angle (D).

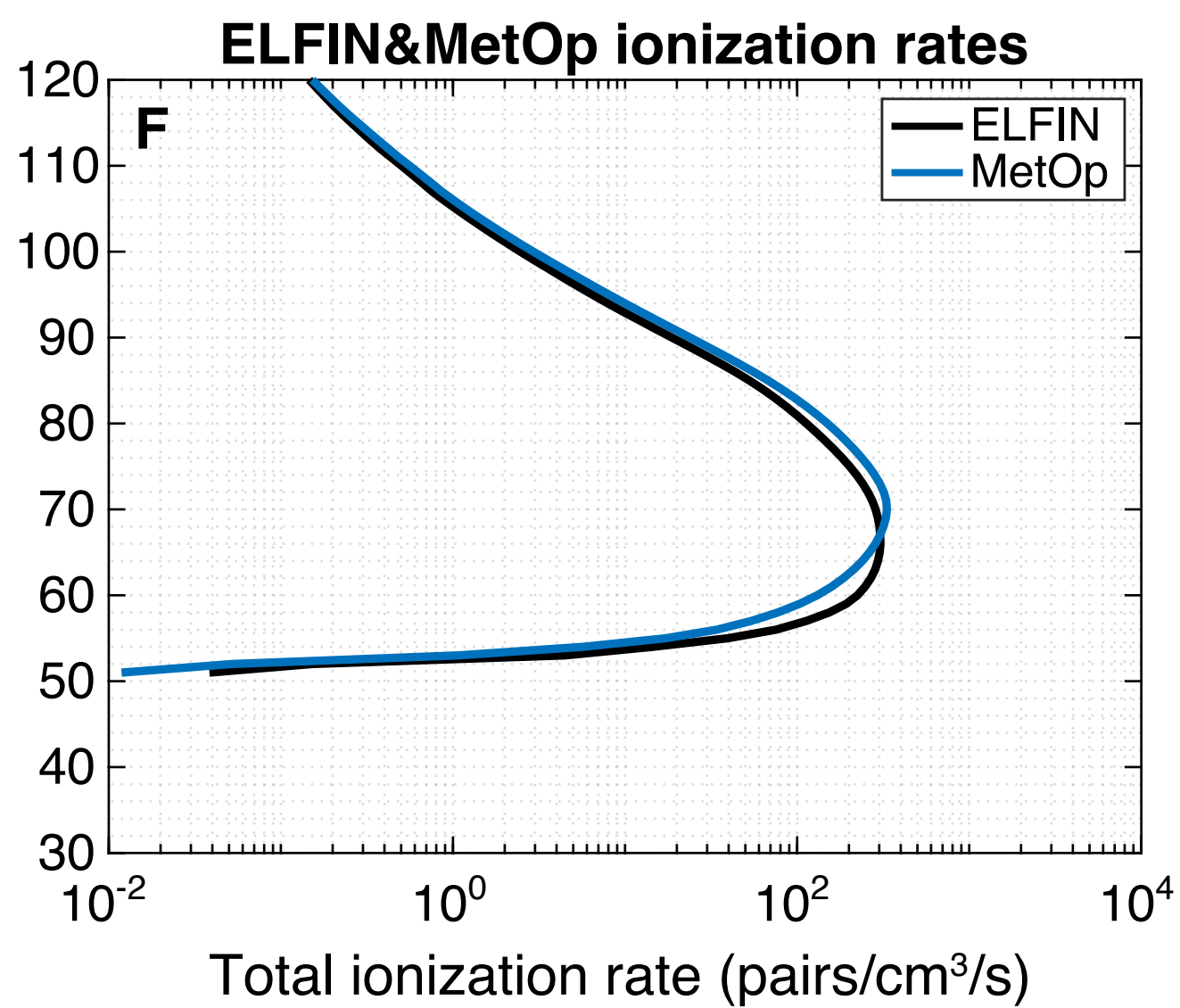
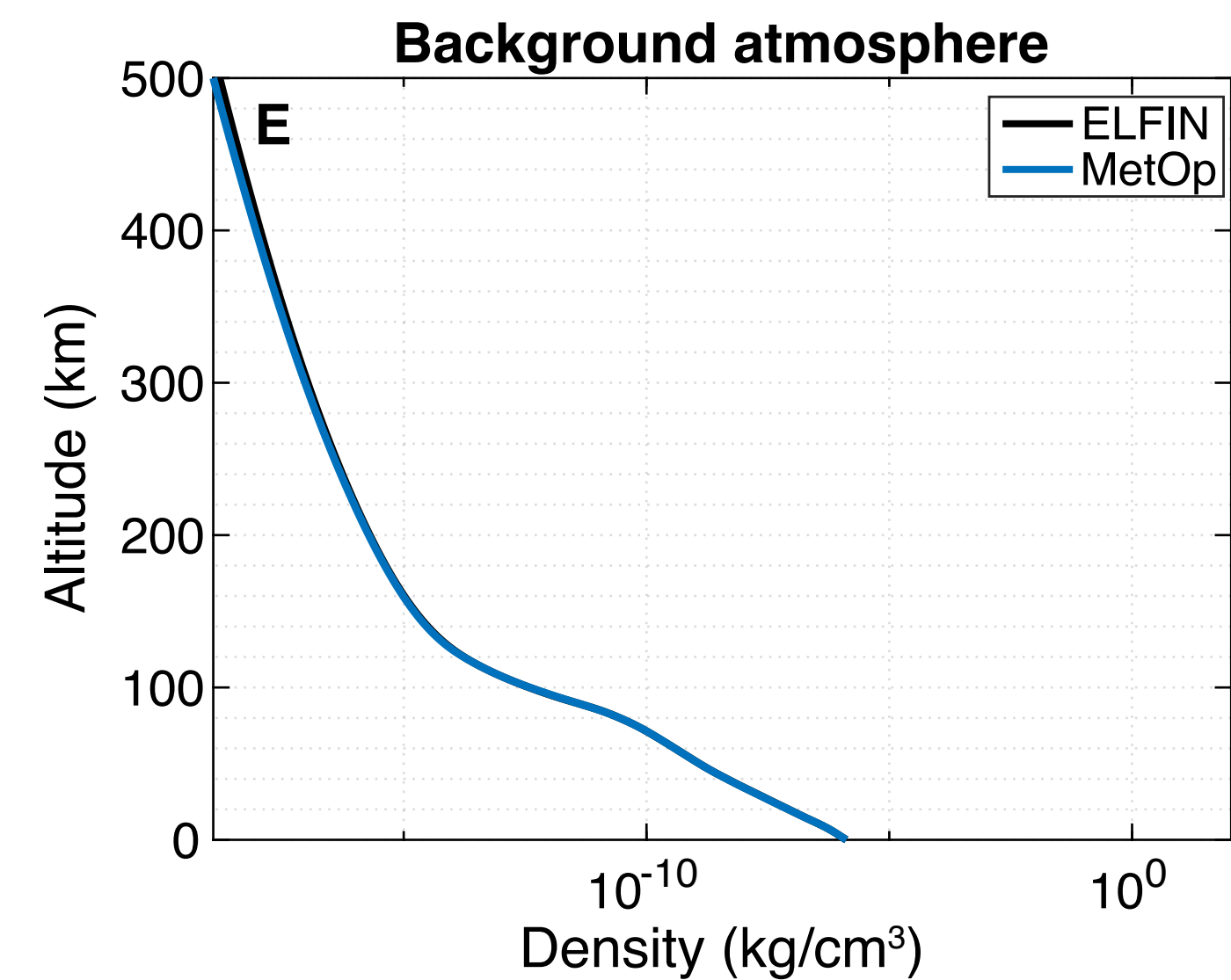
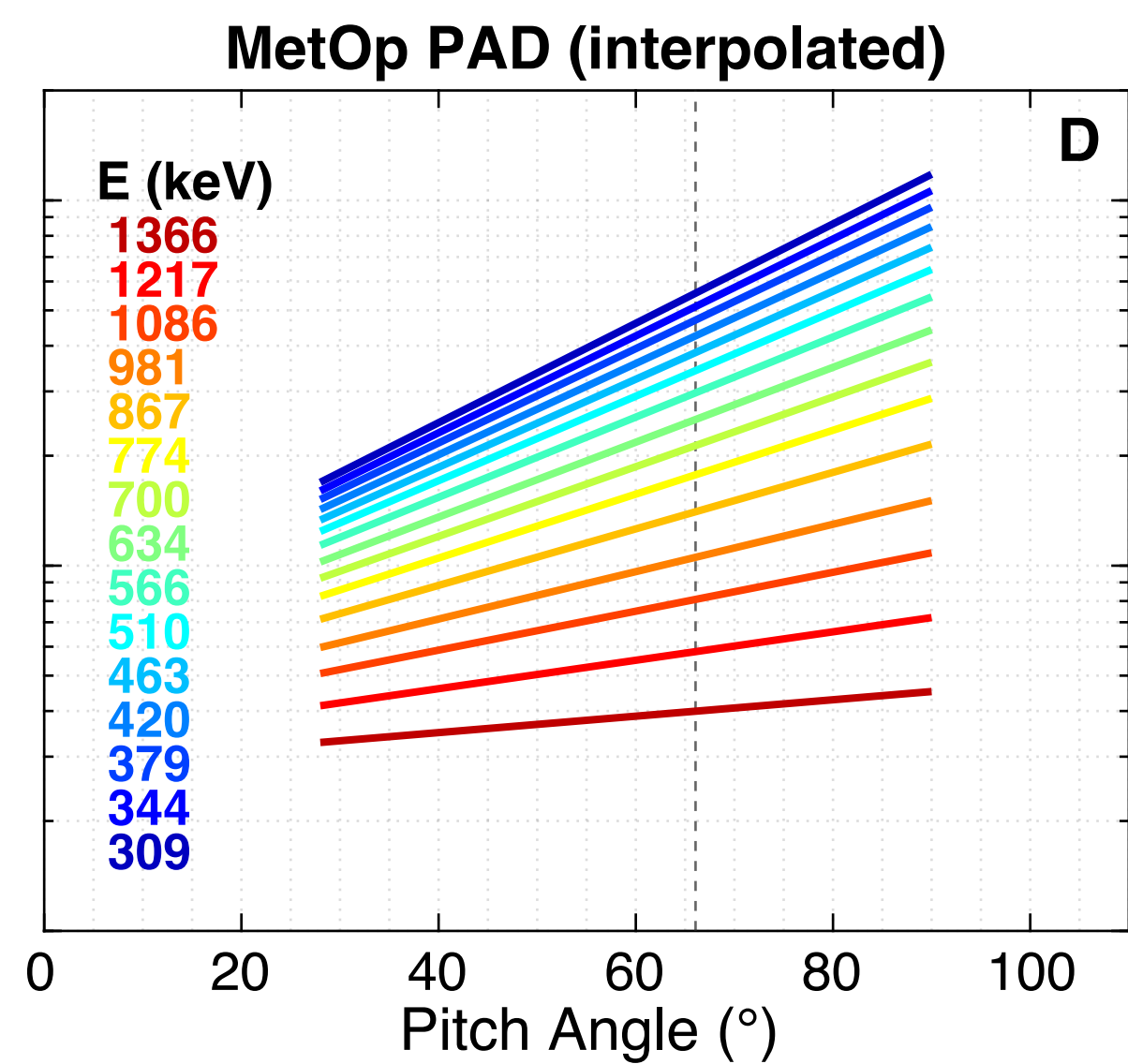
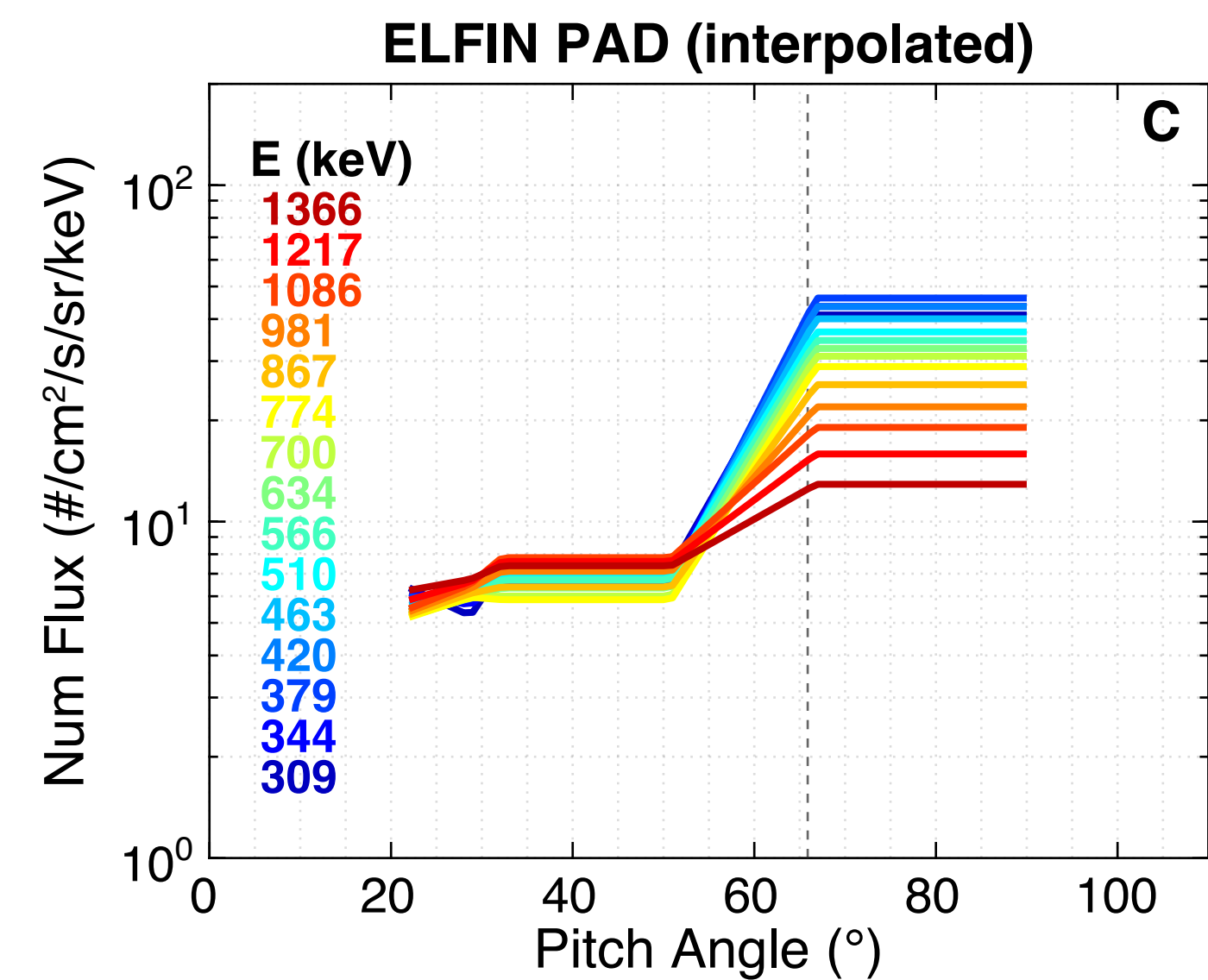
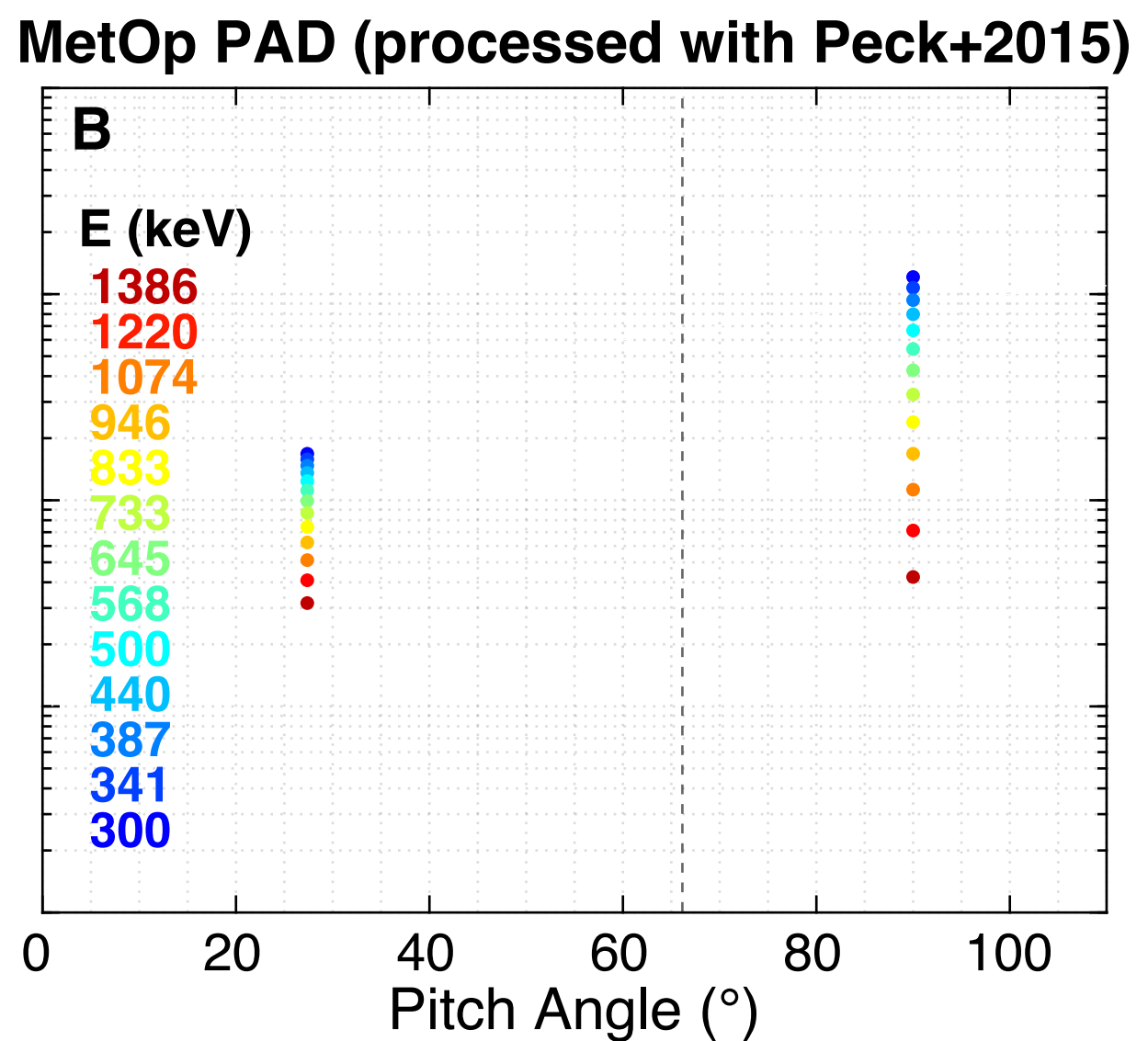
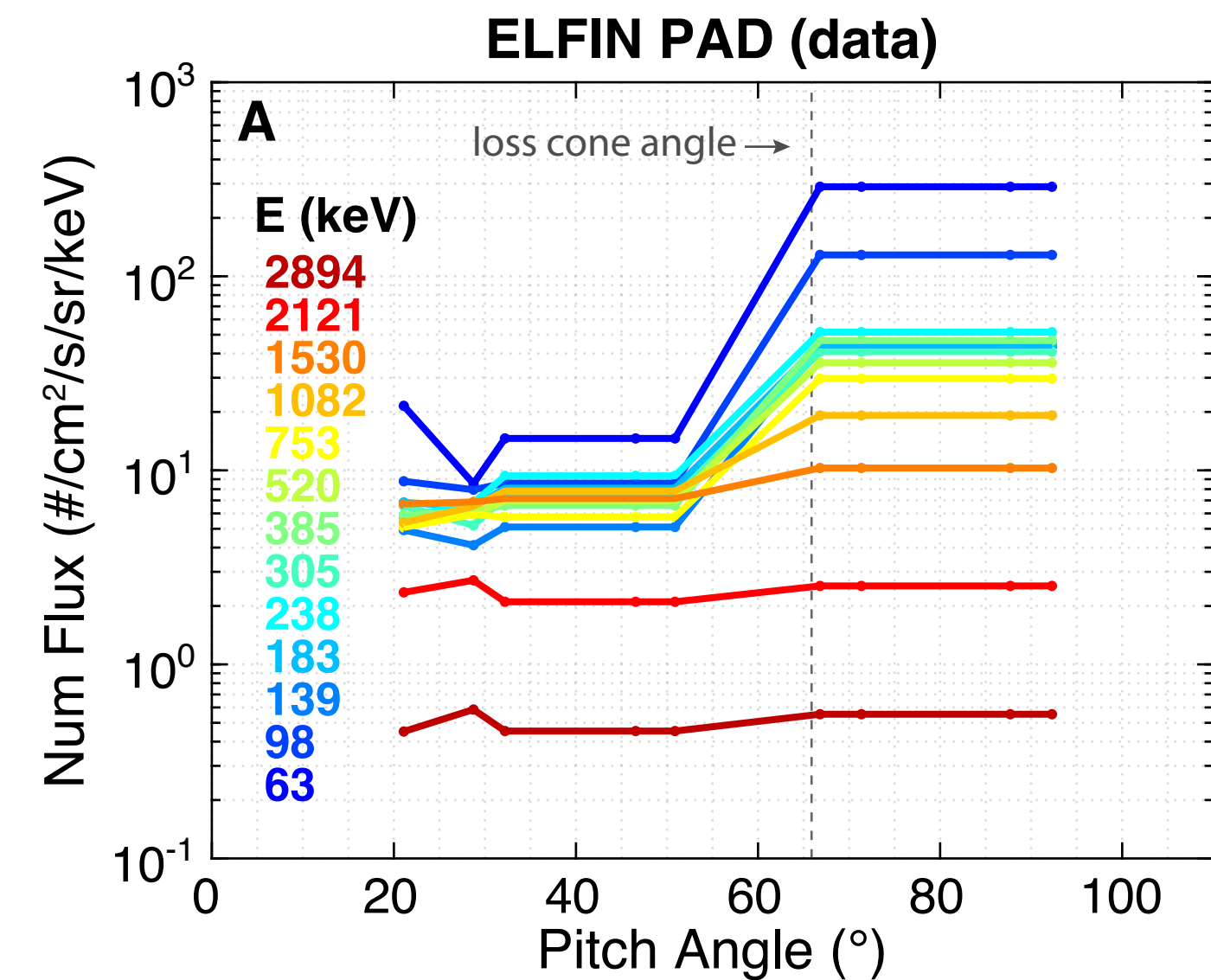
Figure 5: Overview of the ionization rates from BERI due to EMIC-driven EEP. A: range of ionization rates using a PAD as input as described in the legend (e.g., black solid line corresponds to the average PAD shown in Figure 3B; blue solid line corresponds to the result using the minimum PAD from the statistics). Energy deposition is indicated with the additional x-axes at the bottom of panel A (blue for $\text{eV}/\text{cm}^2/\text{s}/\text{km}$ units and maroon for $\text{erg}/\text{cm}^2/\text{s}/\text{km}$ units). B: daily averaged ionization rates recommended by CMIP6 compared to the EMIC-driven BERI ionization rates (black for average PAD and green for median PAD), where MEE: medium-energy electrons, SEP: solar energetic particles, GCR: galactic cosmic rays. The ionospheric E and D-regions are shaded in orange and blue, respectively. The ozone layer is shaded in green with a darker green indicating the approximate altitude of the highest mixing ratio. Atmospheric layers are also indicated.

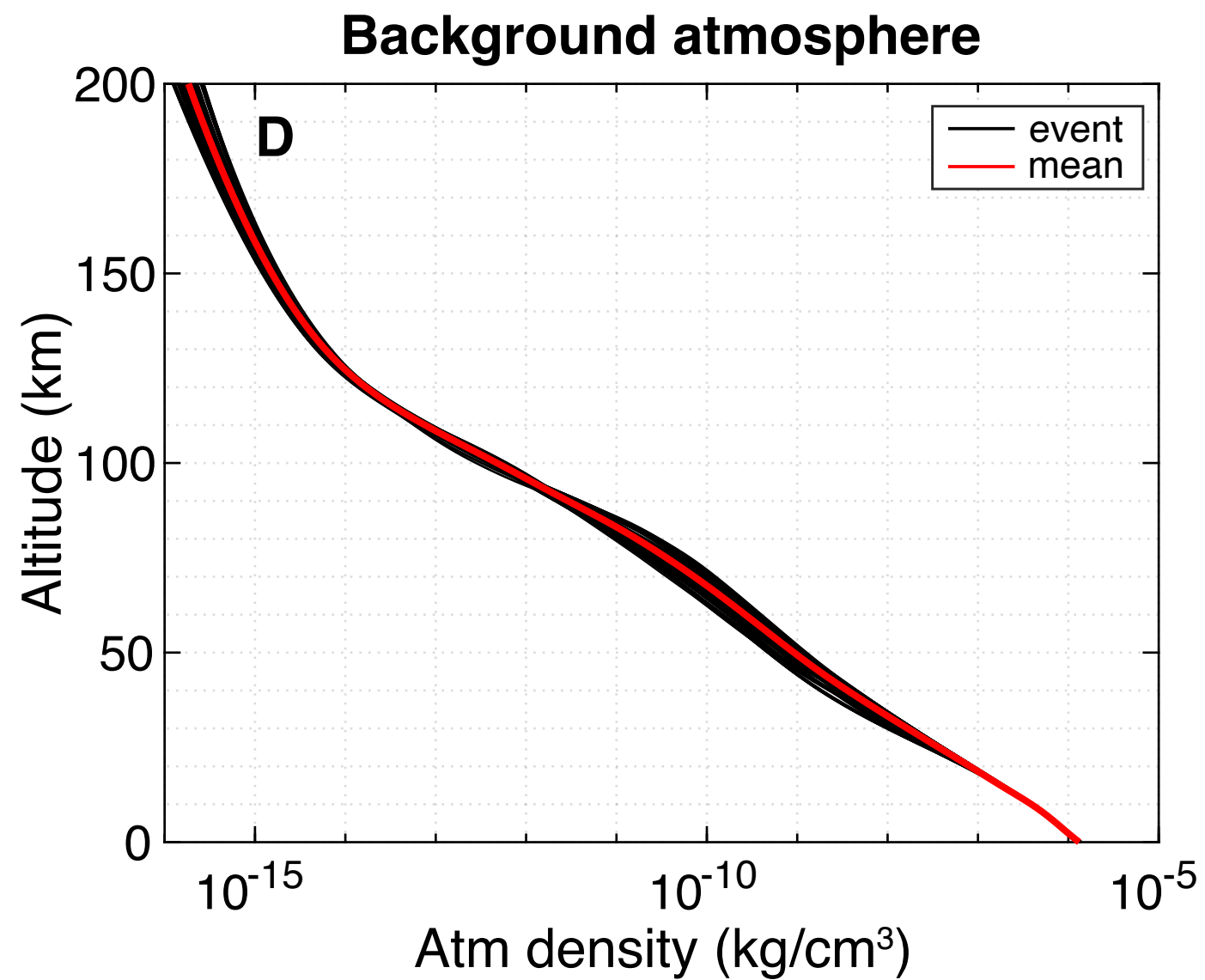
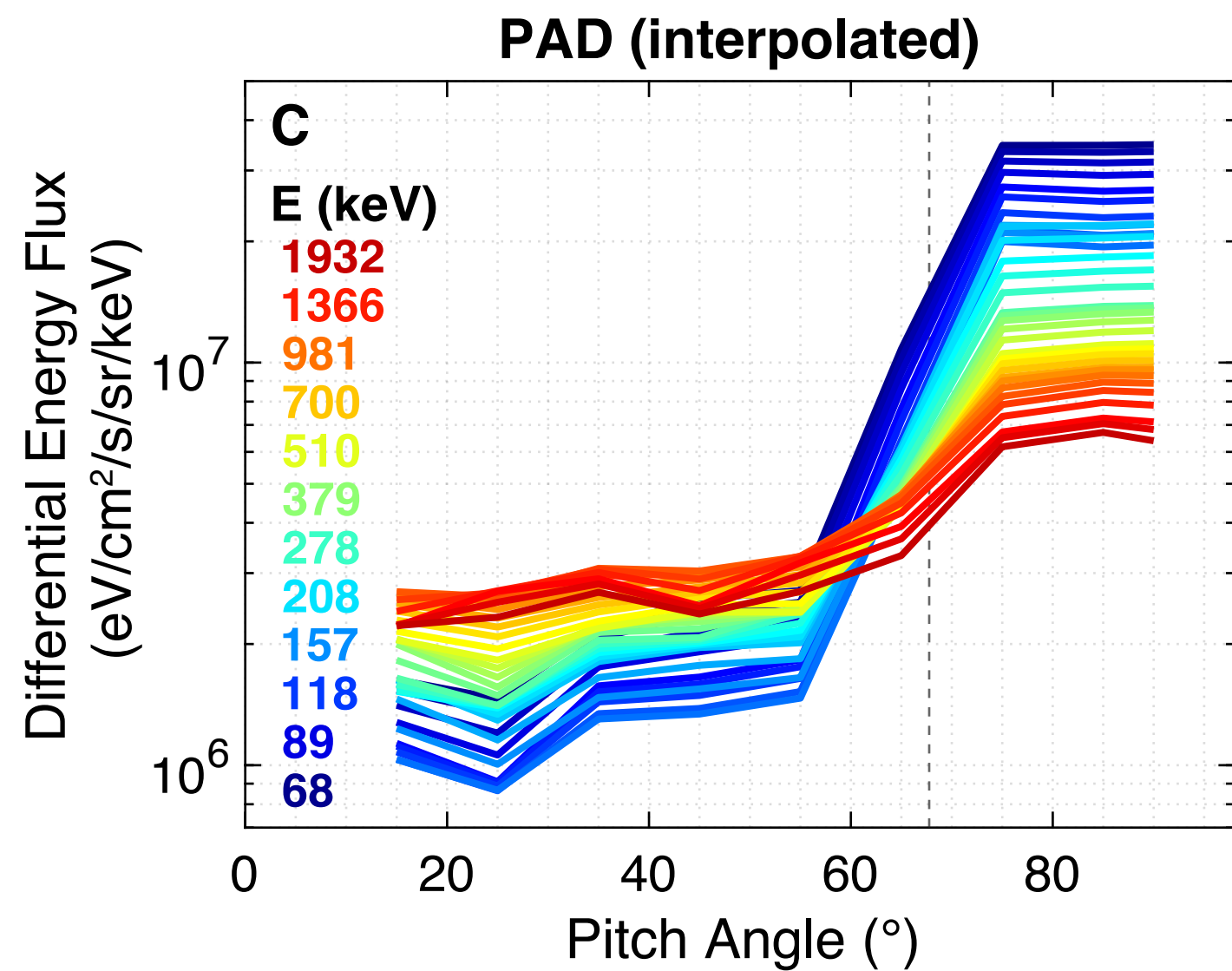
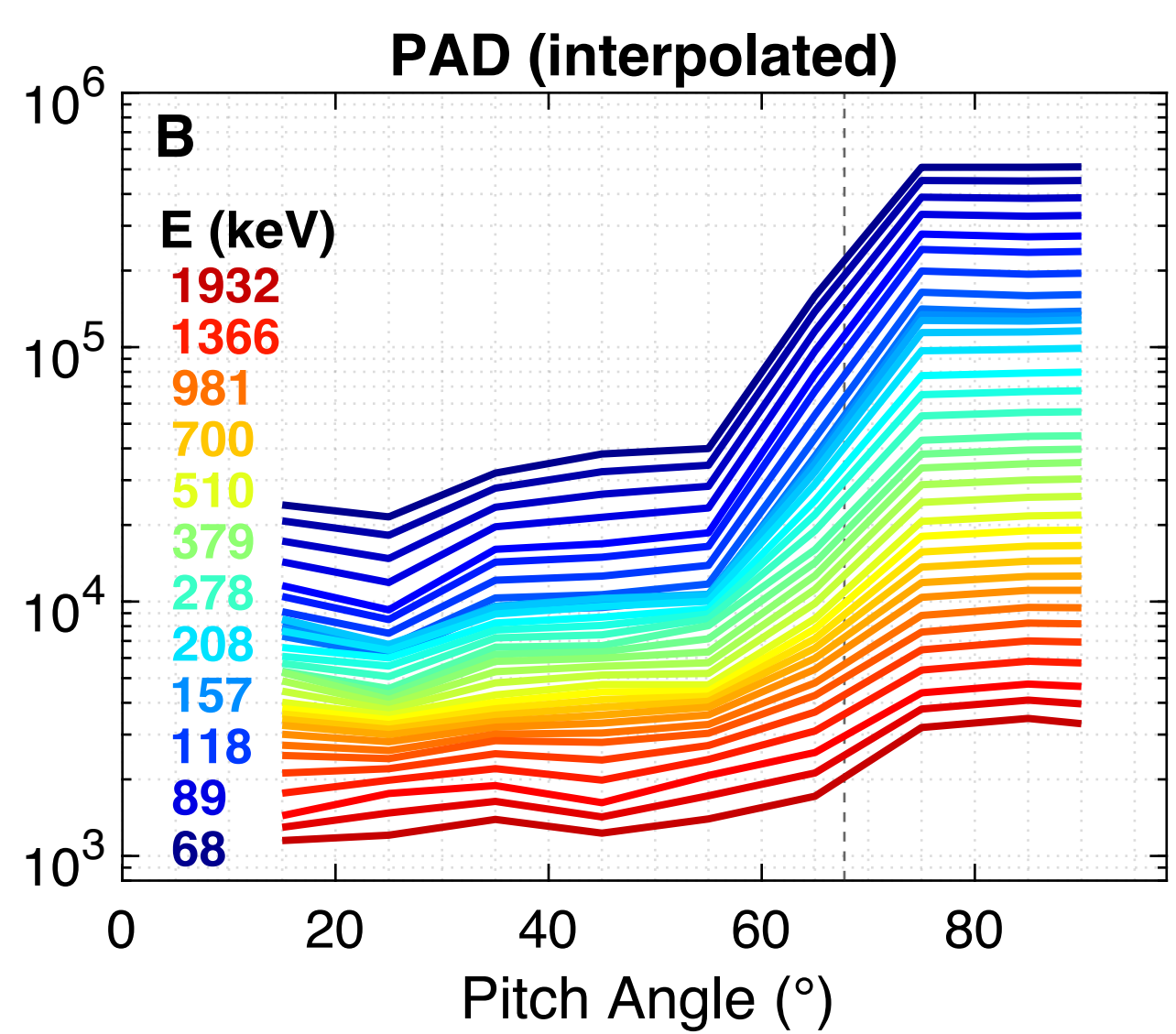
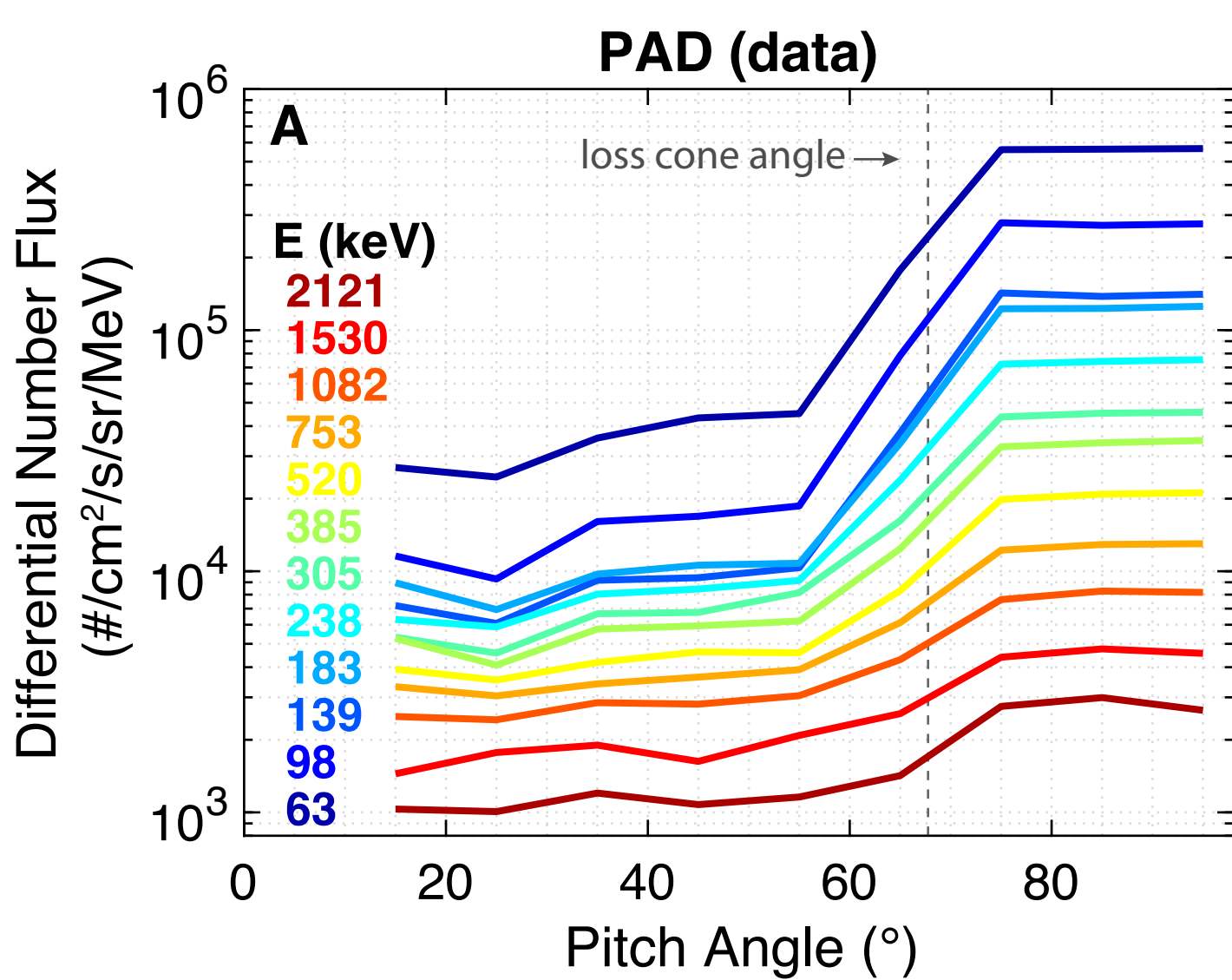
Figure 6: Spatial distribution of the 144 EMIC-driven events in geographical coordinates. Panel A shows the input energy flux calculated for each event from ELFIN data and Panel B shows the ionization energy flux calculated from BERI's ionization rate for each event. The colorbar is in $\text{eV}/\text{cm}^2/\text{s}$ units (black) and $\text{erg}/\text{cm}^2/\text{s}$ units (blue).

Figure 7: Cartoon of the local energy budget: orange arrow indicates the energy input due to EMIC-driven precipitation (calculated from ELFIN data in the loss cone, LC), white dots indicate the ion-electron pairs produced in the mesosphere due to ionization, with the

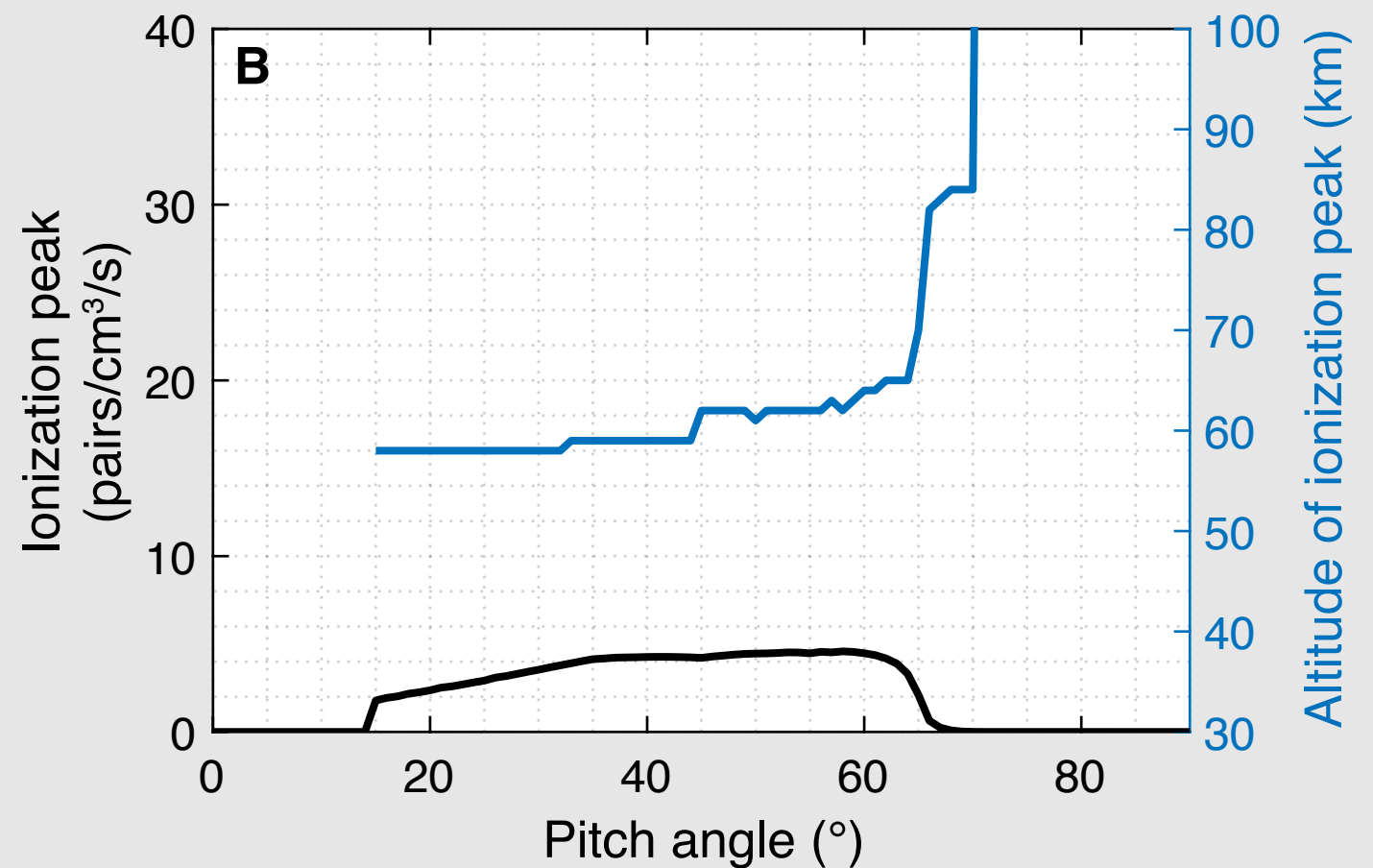
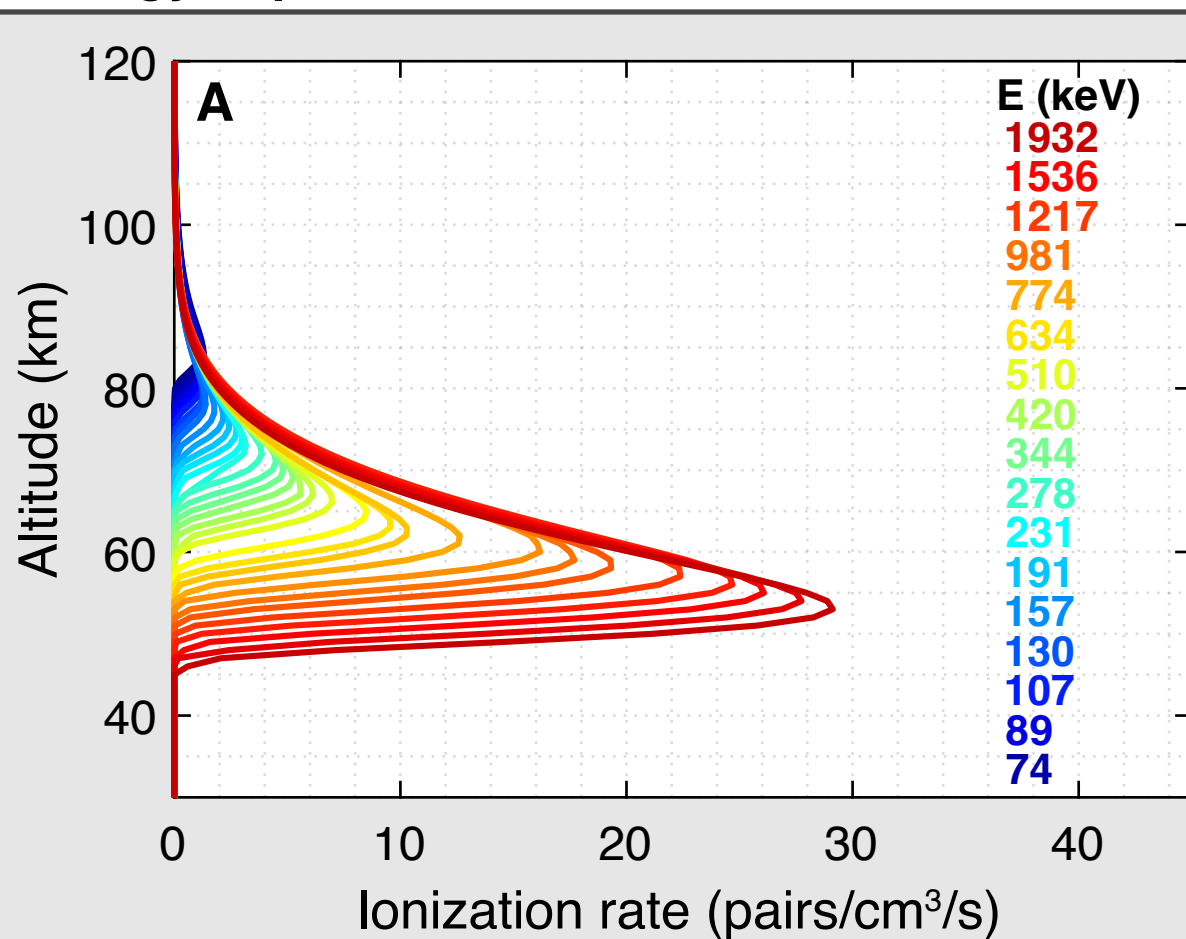
1011 corresponding atmospheric ionization energy flux (calculated from the BERI's ionization rate),
1012 and the pink arrow shows the backscattered energy flux (from BERI's estimate).



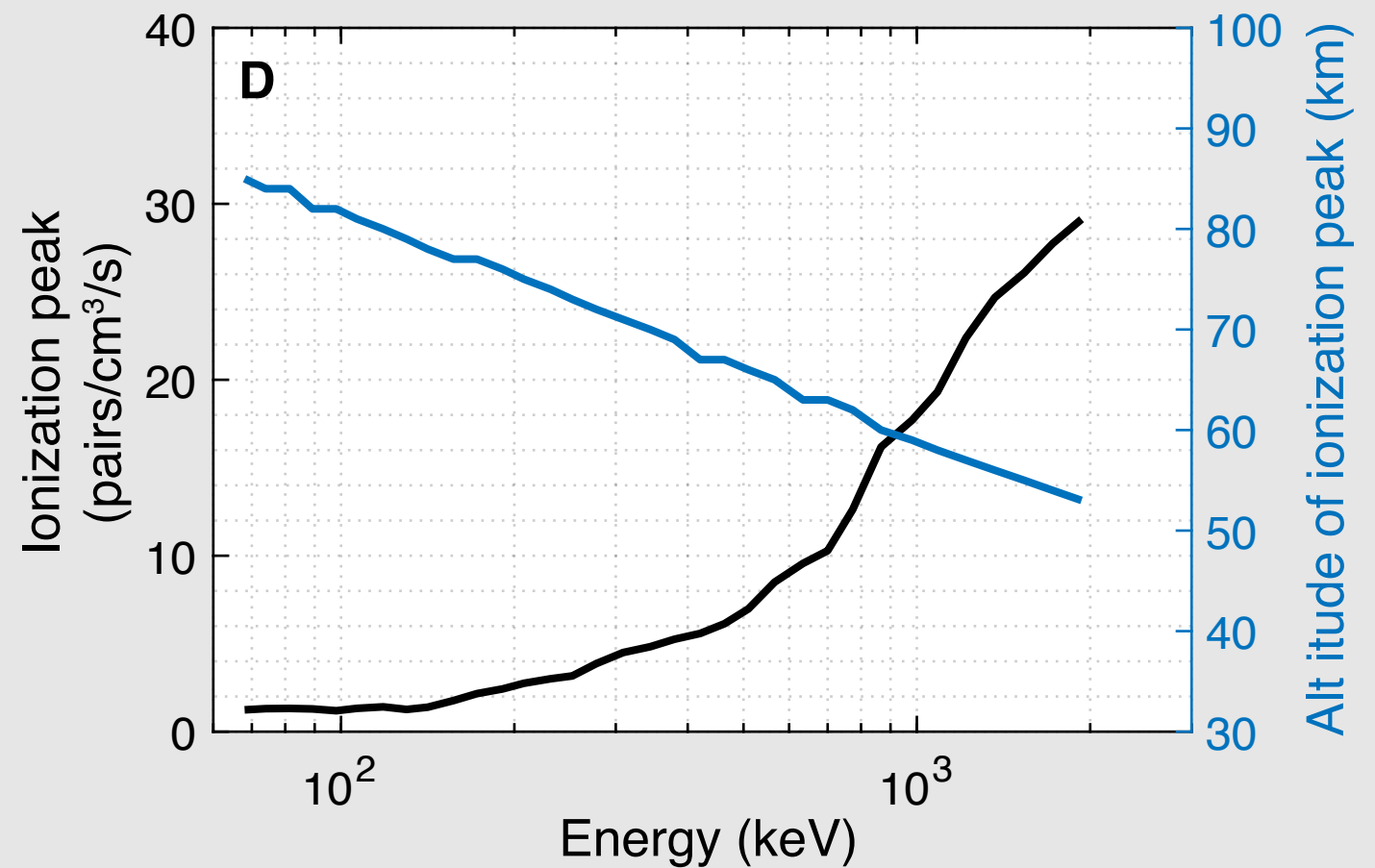
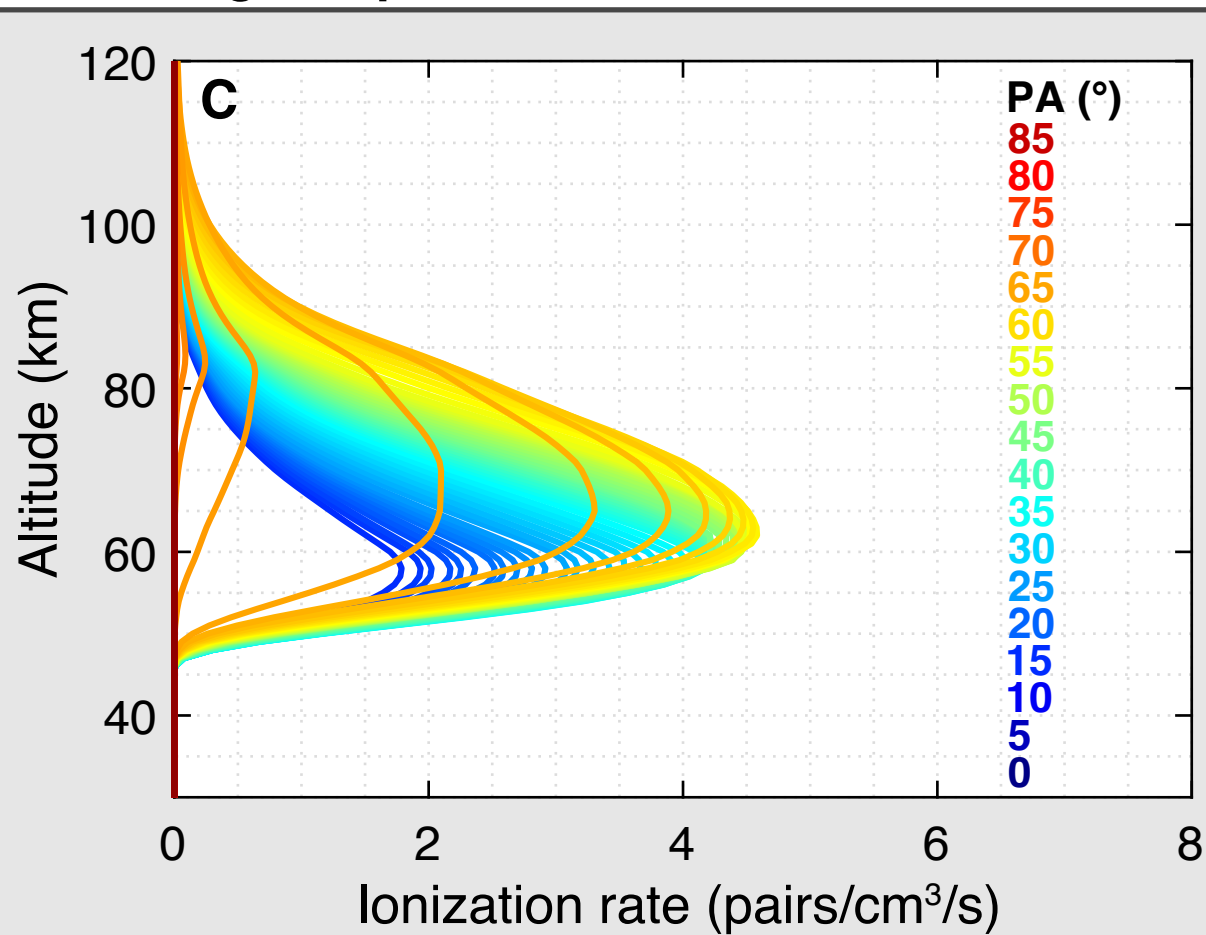




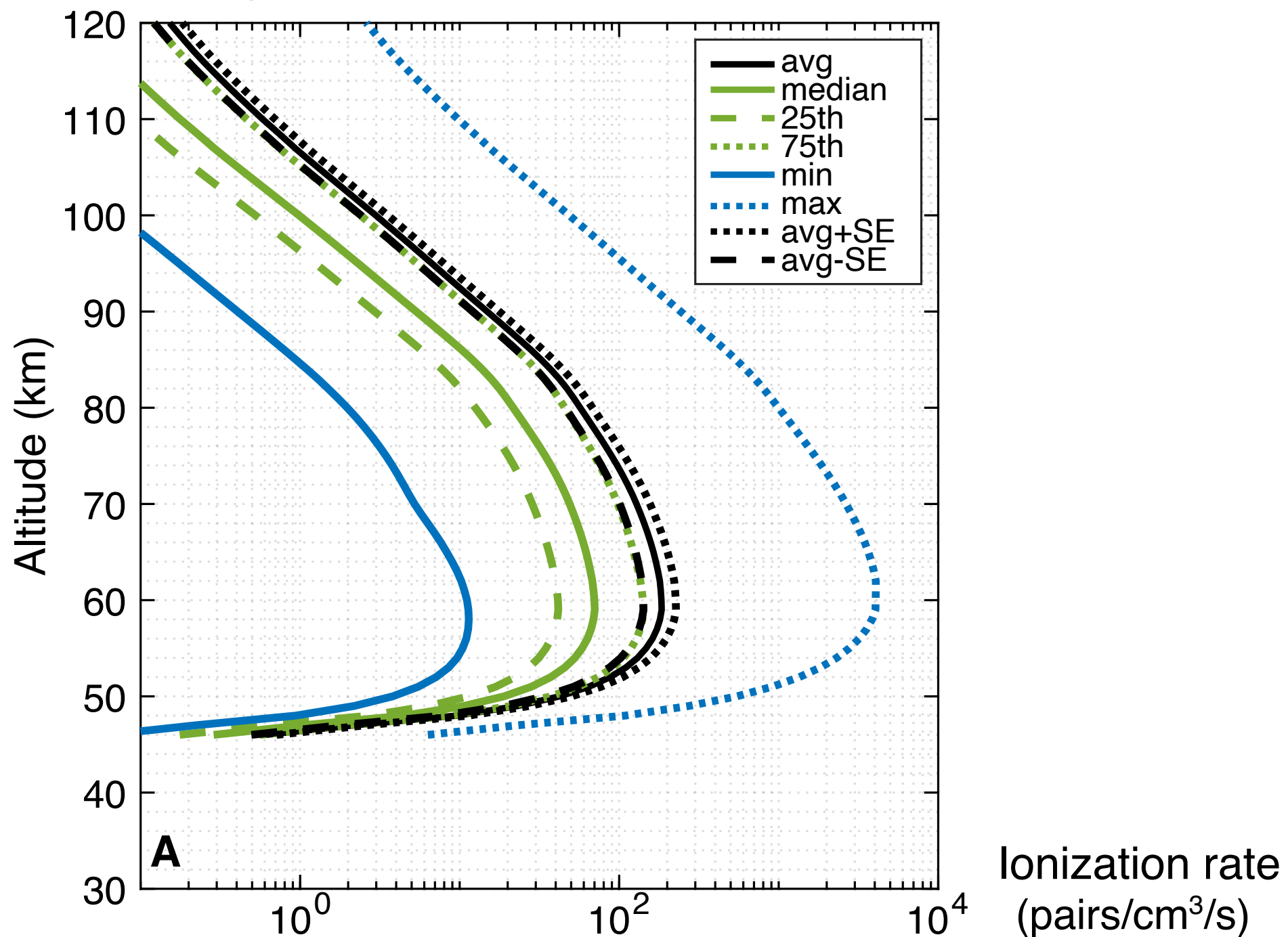
Energy dependence



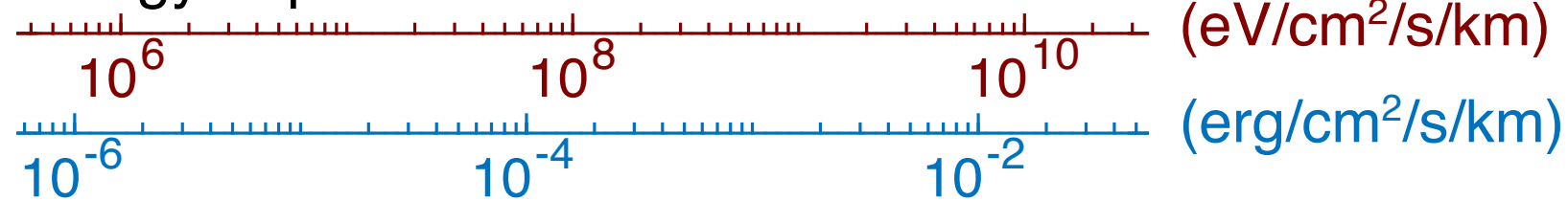
Pitch-angle dependence



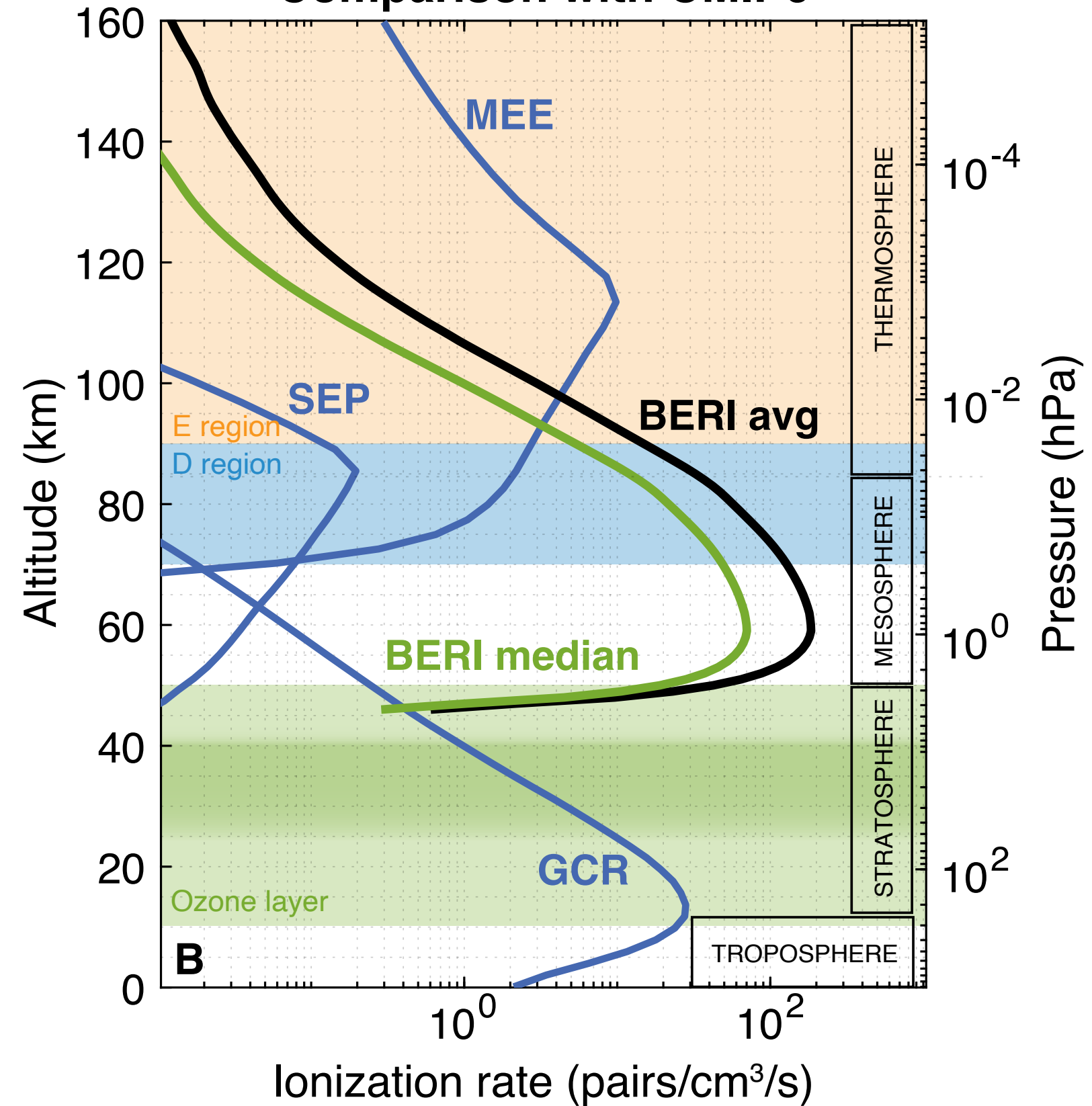
Range of EMIC-driven ionization rates



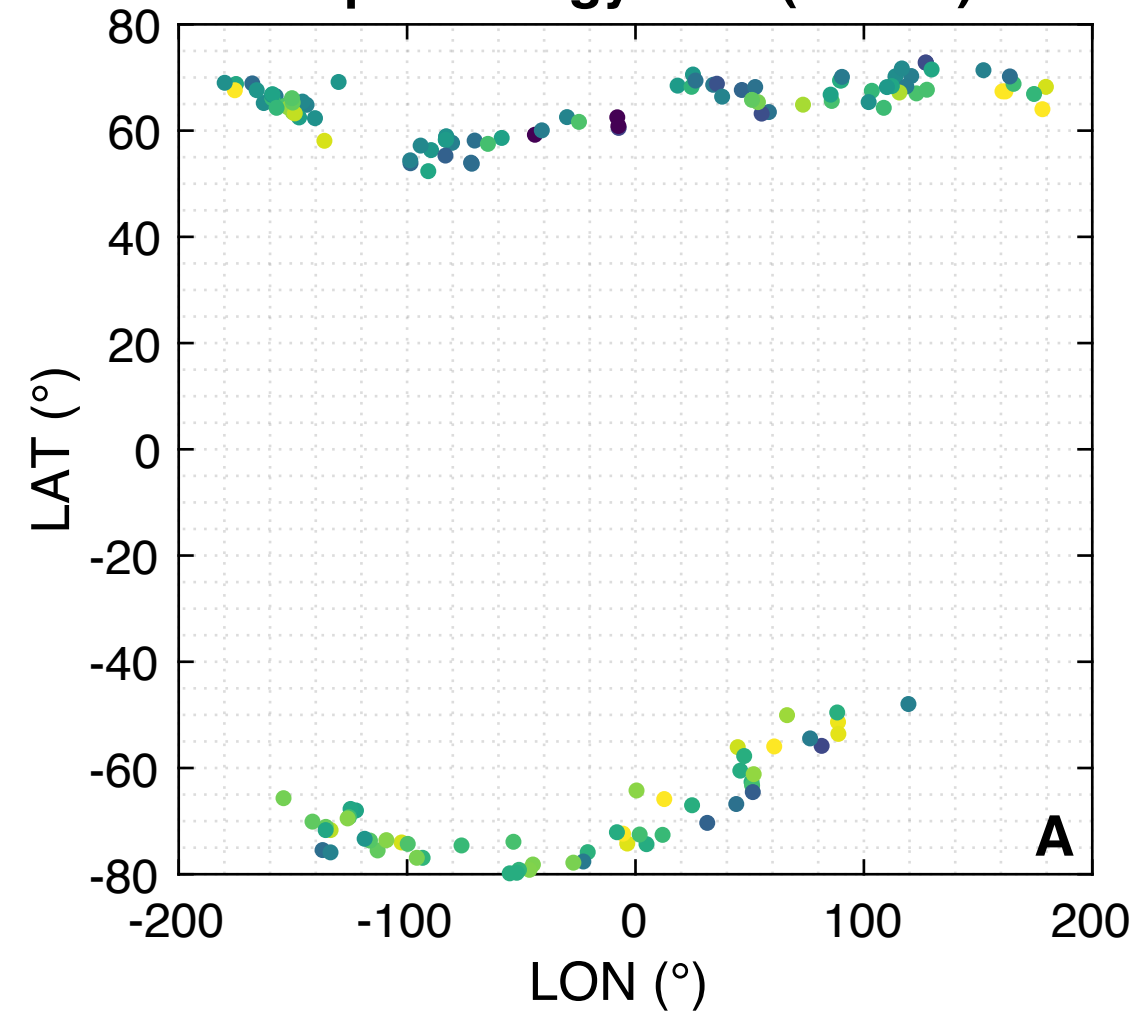
Energy deposition



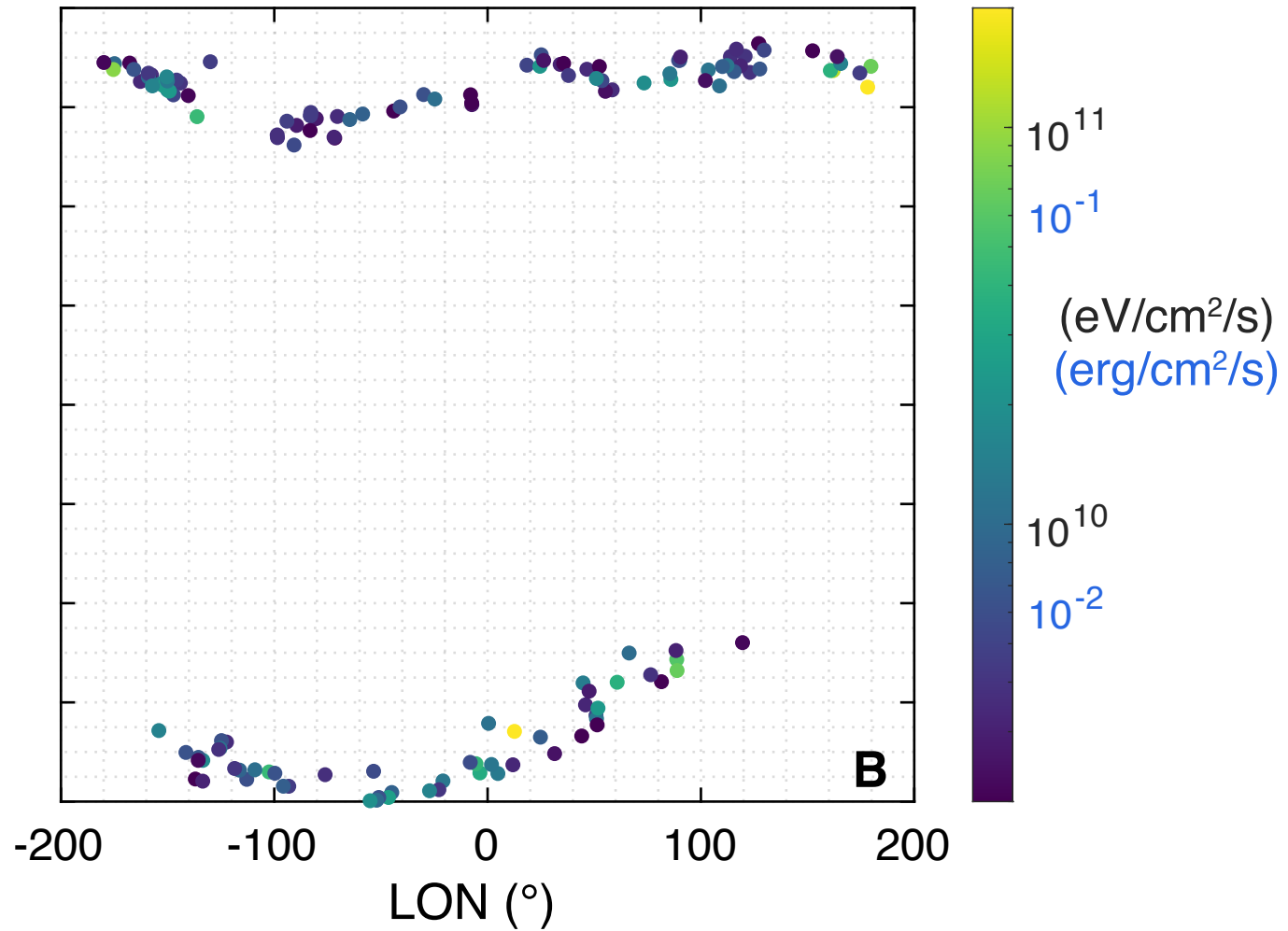
Comparison with CMIP6



Input Energy Flux (ELFIN)



Ionization Energy Flux (BERI)



The diagram illustrates the energy flux in the mesosphere. A green curved line at the bottom represents the Earth's surface. Above it, two concentric dotted blue lines delineate the STRATOSPHERE and MESOSPHERE layers. An orange arrow labeled 'EMIC-driven (LC) INPUT' points from the top left towards the center. A pink arrow labeled 'Backscattered OUTPUT' points from the center towards the top right. In the center of the mesosphere, a cluster of white dots represents ionization, with labels i^+ and e^- nearby. Text labels indicate the energy flux values and their sources: $\sim 0.033 \frac{\text{erg}}{\text{cm}^2 \text{s}}$ from ELFIN for the input, and $\sim 0.008 \frac{\text{erg}}{\text{cm}^2 \text{s}}$ from BERI for the output. A central text block states that $\sim 0.025 \frac{\text{erg}}{\text{cm}^2 \text{s}}$ ionizes the mesosphere, which is approximately 74% of the input energy flux, also from BERI.

EMIC-driven (LC) INPUT

$\sim 0.033 \frac{\text{erg}}{\text{cm}^2 \text{s}}$
||from ELFIN||

Backscattered OUTPUT

$\sim 0.008 \frac{\text{erg}}{\text{cm}^2 \text{s}}$
||from BERI||

$\sim 0.025 \frac{\text{erg}}{\text{cm}^2 \text{s}}$ ionizes mesosphere
(~74% of input energy flux)
||from BERI||

STRATOSPHERE

MESOSPHERE